Remote Distribution of a Mode-locked Pulse Train with Ultralow Jitter

by

Yi-Fei Chen

B.Sc., Peking University, 2003

A THESIS SUBMITTED IN PARTIAL FULFILMENT OF
THE REQUIREMENTS FOR THE DEGREE OF

Master of Science

in

The Faculty of Graduate Studies

(Physics)

The University Of British Columbia

September 2006

Abstract

Remote transfer of an ultralow-jitter microwave frequency reference signal is demonstrated using the pulse trains generated by the mode-locked fiber laser. The timing jitter in a ~ 30 m fiber link is reduced to sub-40 attoseconds (as) integrated over a bandwidth from 1 Hz to 10 MHz via active stabilization which represents significant improvement over previously reported jitter performance. results. An all-optical generation of the synchronization error signal and an accompanying out-of-loop optical detection technique are applied to verify the jitter performance.

Table of Contents

Abstract ii

Table of Contents iii

List of Tables v

List of Figures vi

Acknowledgments viii

Dedication ix

Chapter 1 Introduction to remote synchronization 1

Chapter 2 Background 5

2.1 Mode-locked EDFL 6

2.1.1 P-APM 7

2.1.2 Non-soliton regime and dispersion management 10

2.2 Femtosecond frequency combs 16

2.3 Remote synchronization techniques 19

2.3.1 Microwave and optical frequency distribution 19

2.3.2 Previous experimental schemes and setups 19

2.4 Standard measurement techniques of jitter 23

2.4.1 Allan deviation 23

2.4.2 Phase noise spectral density 24

2.4.3 Timing jitter 26

2.4.4 Intensity cross correlation: non-collinear approach . . 27

Chapter 3 All-optical synchronization by spectral leveraging 30
3.1 Spectral leveraging technique (scheme 1) 31
3.2 experimental setup for spectral leveraging measurement . . . 35
3.3 In-loop jitter measurement for scheme 1 40

Chapter 4 All-optical synchronization by optical heterodyne 44
4.1 Simple optical heterodyne technique (scheme 2) 45
4.2 experimental setup for optical heterodyne measurement . . . 46
4.3 In-loop jitter measurement for scheme 2 48

Chapter 5 Out-of-loop jitter measurement 50
5.1 All-optical timing jitter measurement: collinear approach . . 51
5.1.1 Interferometric cross-correlation (ICC) 54
5.1.2 ICC using two photon absorption in Si-APD 58
5.1.3 Fast Fourier transform on time signal 63
5.1.4 All-optical jitter measuring setup 65
5.2 Experimental results 67
5.2.1 Scheme 1: spectral leveraging 68
5.2.2 Scheme 2: simple optical heterodyne 73
5.2.3 Improvements offered by all-optical approaches 75

Chapter 6 Project summary and future work 77
6.1 Summary 78
6.2 Transferring reference signal through longer fiber 78
6.3 Improving all-optical measurement by using birefringent filter 79
6.4 Locking repetition rates of two mode-locked lasers 82

Bibliography 83

List of Tables

2.1 Rare-earth doped fiber amplifiers: λ_s is the operating wavelength; λ_p is the practical pumping wavelength. 7

5.1 Common semiconductor materials: (a) part of the Periodic Table where semiconductors occur; (b) elemental and compound semiconductors 60

List of Figures

2.1 Energy level of Er^{3+} doped silica fiber 8
2.2 The photo of Er^{3+} doped fiber laser 8
2.3 Principle of polarization additive pulse mode-locking (P-APM) 10
2.4 Experimental configuration of Er^{3+} doped fiber ring cavity laser 11
2.5 Round-trip time (T) of the EDFL vs. wavelength (λ) 16
2.6 The representation of the ultrashort pulse in the time domain (pulse train) and frequency domain (frequency comb) 17
2.7 Long-Sheng Ma's remote synchronization scheme in 1994 . . 20
2.8 Kevin Holman's remote synchronization scheme in 2005 . . . 22
2.9 Schematic setup for the timing jitter measurement by intensity cross-correlation 28

3.1 All-optical generation of an error signal for synchronization by optical leveraging (Scheme 1) 31
3.2 Experimental setup for spectral leveraging scheme (scheme 1) 36
3.3 Spectra of reference and transmission paths and interference between them; Spectral slices at two extremes 39
3.4 In-loop measurement of jitter spectral density and integrated jitter for spectral leveraging (scheme 1) and the noise floor . . 40

4.1 All-optical generation of an error signal for synchronization by simple optical heterodyne (scheme 2) 45
4.2 Experimental setup for jitter cancellation with single optical heterodyne (scheme 2) 47

4.3 In-loop jitter measurement of jitter spectral density and integrated jitter when synchronized by simple optical heterodyne (scheme 2) and the noise floor 48

5.1 The numerical simulation of the interferometric cross-correlation signal and the 1st order derivative thereof in the vicinity of time delay equal to zero. 58
5.2 Typical silicon photodiode structure for photoconductive operation 59
5.3 Spectral response of the Si-APD at 25°C 61
5.4 Experimental configuration of the interferometric cross-correlation measurement 66
5.5 Auto-correlation measurement of pulse widths of reference and transmitted arms in time domain 67
5.6 Simulated interferometric cross-correlation pattern 69
5.7 Timing jitter measurement by scope with interferometric cross-correlation 71
5.8 All optical out-of-loop jitter measurement for synchronized by spectral leveraging (scheme 1) 73
5.9 All optical out-of-loop jitter measurement for synchronized by simple optical heterodyne (scheme 2) 74
5.10 Unlocked noise and noise floors of microwave and optical detection 75

6.1 Experimental setup for interferometric cross-correlation detection by using birefringent filter 80

Acknowledgments

I would like to give my gratitude to all the members of the Laboratory of Ultrastable Femtosecond Optics for their generous assistance throughout the process of my M.Sc. thesis research. Special thanks for my supervisor, Dr. David Jones, for his support and guidance of my research work. He is always patient to listen to me and I enjoy the working time in the lab and game time on the loan beside SUB and on the paintball field during the past two years. David's kindness and optimism is a trait which I have admired, and hope to mimic in the future if at all possible.

I would also like to thank Dr. Jie Jiang for helping a lot in my project. He is always available in the lab for my huge amount of questions when David is not during the winter sessions.

I would also like to show my deepest appreciation for the experimental advices from and discussions with Dr. Kirk Madison, Sibyl Drissler, Vivide Chang, TJ Hammond and many other colleagues.

I extend thanks also to my family, to my girlfriend, Jessica Wen-Chuan Zhou, as well as to my best friends Ri-Chu and Jin-Ming, who have been both patient and supportive throughout this study.

To Xun-Yuan, Kai-Rong, and Jessica

Yi-Fei Chen

Chapter 1

Introduction to remote synchronization

The traditional method for transferring frequency standards uses the Global Positioning System (GPS) [1]. Long averaging times (~days) are necessary in this approach to average out environmental fluctuations in signal paths from satellites. However, these GPS-based systems will not be able to leverage the high-stability, low-averaging times of next generation optical atomic clocks [2],[3]. A good candidate for remote distribution of frequency references derived from optical atomic clocks is optical fiber links. Such transmission facilitates the comparisons of relative instability and systematic drifts between different frequency standards. In a word, the most important motivation of this work is to keep the stability of transferring the optical and radio frequency standards above the stability of the state-of-the-art optical clock. There are also a number of applications that would benefit from the transmission of ultra-low jitter timing signals. One such application is long-baseline interferometry for radio astronomy [4]. Low-jitter transfer of a frequency reference from a maser oscillator could be used to distribute it to each telescope in an array of ~ 60 radio telescopes over a distance of ~ 20 km. This would enable all telescope in an array to collect data phase-coherently, therefore, simulating a single telescope with a very large aperture. In this application, the phase noise of < 38 fs over a bandwidth from 1 Hz to 10 MHz for transferring a signal in the frequency range of $27 \sim 142$ GHz is required. Low-jitter transfer can be also used for distribution of timing signals throughout a linear accelerator facility used to produce ultrashort X-ray pulses for time-resolved pump-probe experiments [5]. A $< 5\% \times$ pulsewidth timing jitter[1] is expected for the pump-probe experiment. Several other applications, including gravity wave searches and occultation science [6] would also benefit from low-jitter transfer. Previous work [7] has utilized techniques based on microwave detection in order to detect and cancel the noise added during transit down the distribution fiber. However, while working in the microwave domain several sources of noise conspire to limit the achievable jitter to approximately 10 fs including Johnson noise, shot noise, amplifier flicker ($1 / f$) noise and amplitude-to-phase conversion in the detection, amplification, and mixing of the signals. In general, for low signal strength thermal noise and amplitude noise will dominate, and for higher signal strength shot noise and amplitude-to-phase conversion take over [8] .

Some of the limits inherent in using microwave detection can be circumvented by turning to optical detection for generation of the synchronization error signal. This is in part due to the huge lever arm[2] available when optical detection is utilized. A balanced optical cross-correlation setup was used to derive a dispersion-type error signal for local synchronization of a fs Ti:Sapphire laser with a fs Cr:LiSAF laser [9]. Alternatively, a narrow-linewidth cw laser (stabilized to a high-finesse optical cavity) was employed at NIST to optically synchronize two local fs Ti:Sapphire lasers [10]. While in principle both of these techniques could be used to derive an error sig-

[1]For example, the timing jitter is expected to be smaller than 5 fs for a 250 fs pulse.

[2]The huge lever arm means the considerable magnification of $\sim 10^5$ on the synchronization error signal provided by the index number of the optical frequency comb.

nal for remote synchronization, their implementation in this setting would be rather complex. In the former case, near-perfect chirp compensation of the transmitted pulse would be required. The latter case would require stabilized transmission of an optical frequency standard [11].

In my thesis work, two different approaches to all-optical synchronization which are more suitable to applications involving remote synchronization are presented. One of the techniques is also a simple and robust method to synchronize two local femtosecond (fs) lasers as long as there is good spectral overlap between them. Two different all-optical techniques for distributing an ultra-low jitter frequency standard are demonstrated. A high-stability, low jitter rf signal is transmitted over a round-trip $\sim$ 60-m fiber link with a jitter of 11.4 as (1 Hz to 10 MHz) using spectral leveraging scheme. The 2^{nd} scheme, simple optical heterodyne, displays a transmitted jitter of 12.1 as (1 Hz to 10 MHz). This performance is measured by an out-of-loop interferometric cross-correlation setup (ICC) with a greatly reduced noise floor (to 9.7 as) of both the error signal generation and measurement techniques, compared to the technique working within rf regime [7]. The physics in these synchronization and measuring techniques will be explained in detail in chapter 3, 4 and 5.

Chapter 2

Background

In this chapter, a background introduction to various facilities and techniques that are used in my experiment is given. It starts with the mode-locked Er^{3+}-doped fiber laser (EDFL), which runs at 1550 nm and is used as the pulse source in my experiment. The mode-locking scheme for EDFL, polarizing additive pulse mode-locking, and how we measure the dispersion of the fiber is going to be talked. In the section 2.2, the femtosecond frequency comb, which is used as carrier for the radio frequency standards in our experiment, is demonstrated. In the next section, I will introduce several methods for microwave and optical frequency distribution. Two previous experiment on remote synchronization are also briefly described herein. The definitions and application regimes of two classes of the characterization of the stability of a frequency source will appear in the last section.

2.1 Mode-locked EDFL

Although fiber amplifiers were constructed as early as 1964 [12], their extensive use did not begin until the late 1980s when the techniques for fabrication and characterization of low-loss, rare-earth doped fibers were perfected. A rare-earth group consists of a group of 14 elements with atomic numbers in the range from 58 to 71. When these elements are doped into silica, fluoride or other glass fibers, they become triply ionized. The rare-earth doped fiber lasers are attractive due to many advantages. They are solid-state and do not need to be water-cooled, and they can be pumped easily with a

Ion	Host	λ_s (μm)	λ_p (μm)
Tm	Fluoride	0.8	0.875
Nd	Silica	1.08	0.78
Yb	Silica	1.08	0.89
Pr	Fluoride	1.3	1.01
Tm	Fluoride	1.46	1.2
Er	Silica	1.55	0.98, 1.48
Er:Yb	Silica	1.55	1.06
Tm	Silica	1.9	0.79
Ho:Tm	Fluoride	2.054	0.89

Table 2.1: Rare-earth doped fiber amplifiers: λ_s is the operating wavelength; λ_p is the practical pumping wavelength.

wavelength division multiplexing (WDM) fiber coupler and a compact electrical pumped diode pump laser [13]. They are compact and cost-effective. And due to the recent develop of the optical metrology with the optical frequency comb, the long-term stability of the mode-locked doped fiber laser also makes itself a great candidate for novel metrological devices such as optical atomic clocks [14]. A table of the properties of different types of doped fiber amplifiers are given in Table 2.1.

Of the fiber laser, the EDFL has attracted special attention from scientists and engineers as its wavelength matches the 1.55 μm telecommunication window, where propagation losses of $\alpha = 0.2$ dB/km are standard.

2.1.1 P-APM

EDFL can operate in both CW and mode-locking modes. In our experiment, we expect it to run in the latter case, where the output of the EDFL is going to be a train of pulses with a width of $\sim$100 fs.

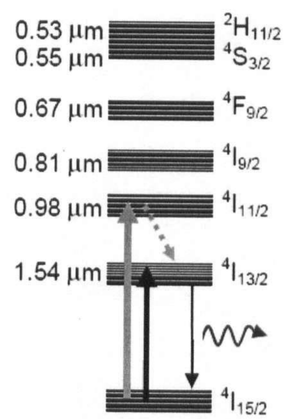

Figure 2.1: Energy level of Er^{3+} doped silica fiber. Two possible pump wavelengths are 980 nm and 1480 nm, which are shown in this figure. The laser transition ${}^4I_{13/2} \longrightarrow {}^4I_{15/2}$ terminating in the ground state of the Er^{3+} ion generates the laser radiation at 1.54 nm.

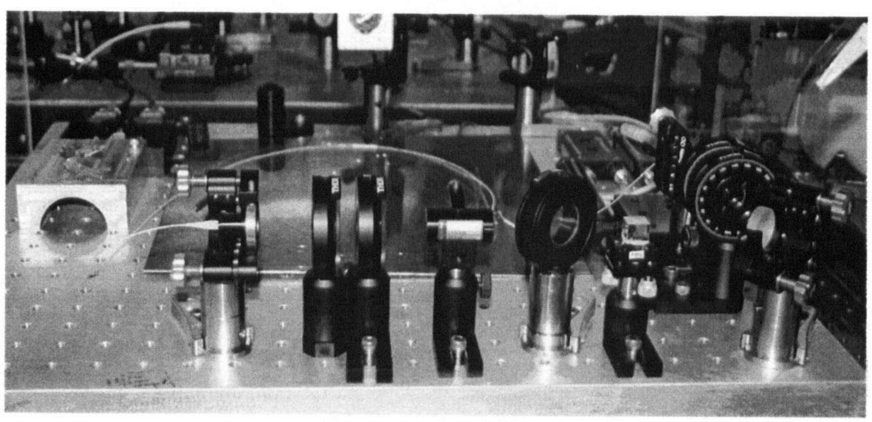

Figure 2.2: The photo of Erbium-doped fiber laser (EDFL) used in this experiment and mode-locked by Polarization Additive Pulse mode-locking (P-APM). The glowed green light from the Er^{3+} doped fiber is the up-conversion emission due to excited-state absorption (ESA).

Fig. 2.2 shows the setup of my EDFL, which is a unidirectional ring cavity fiber laser and applies the so-called polarization additive pulse mode-locking (P-APM) scheme to realize mode-locking [15],[16],[17]. The APM technique employs a nonlinear interferometer to realize pulse shortening. The beam is split into two arms with an nonlinear element in one arm. The pulse is recombined at the output of the interferometer and pulse shortening occurs through the coherent addition of the phase-modulated pulses. Thus the phase modulation is transformed to be a amplitude modulation. APM is easily realized in fiber lasers due to strong nonlinear effects such as self phase modulation (SPM) that arise from the small mode field diameter of the fiber. The special scheme used in fiber laser is called polarization additive pulse mode-locking since left- and right-hand circular polarization components experience different nonlinear phase shift and are added together at the final polarizer. The orientation of the polarization is rotated by the nonlinear medium. The amount of rotation depends on the intensity of the light. Therefore by lining up the polarizer with the polarization of the central peak of the pulse, pulse shortening is achieved (see Fig. 2.3).

In the passive mode-locked fiber laser, the laser will evolve into the pulsed mode on its own without an external perturbation or trigger. This is called self starting, meaning that the pulses start up from an initial noise fluctuation. It has been shown experimentally and theoretically that the mode-pulling and spatial hole burning will make the self-starting difficult. By configuring unidirectional ring fiber laser [19], the etalon that possibly exists between one end of fiber and an end mirror in the linear cavity is extinguished and the resulting standing wave due to the interference between

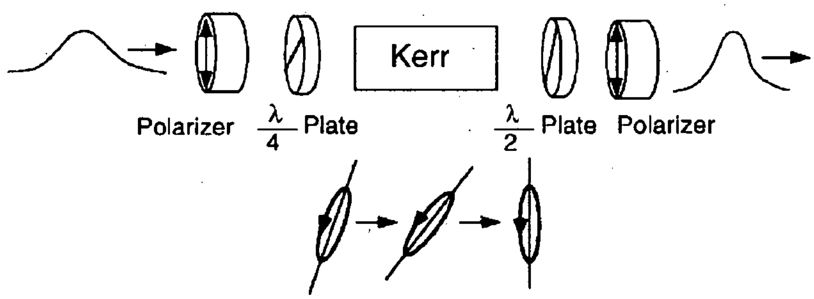

Figure 2.3: Realization of pulse shortening in a EDFL through polarization additive pulse mode-locking (P-APM). A pulse is initially linearly polarized and then made elliptically polarized with a quarter-wave plate. The light then passes through an optical fiber when ellipse rotation occurs and the peak of the pulse rotates more than the pulse wings. At the output of the fiber, the half-wave plate orients the pulse so that the peak of the pulse passes through the polarizer while he wings of he pulse are extinguished, thus achieving pulse shortening [18].

the forward and backward propagating beams in the linear cavity is also limited. So it is easier to get a self passive mode-locked fiber laser self started in the unidirectional ring cavity laser, which we used in our experiment.

2.1.2 Non-soliton regime and dispersion management

As for the unidirectional ring fiber lasers that apply P-APM scheme to realize mode-locking, they can run in soliton and non-soliton regime. The word soliton refers to a special kind of wave packets that can propagate over a long distance without distortion [20]. In fiber optics, the solitons exist due to a balance between SPM and anomalous dispersion. Fig. 2.4 shows the setup sketch of the stretched pulse laser, which runs in the non-solition regime and is used in our experiment to generate $\sim$ 100 fs pulse trains. The

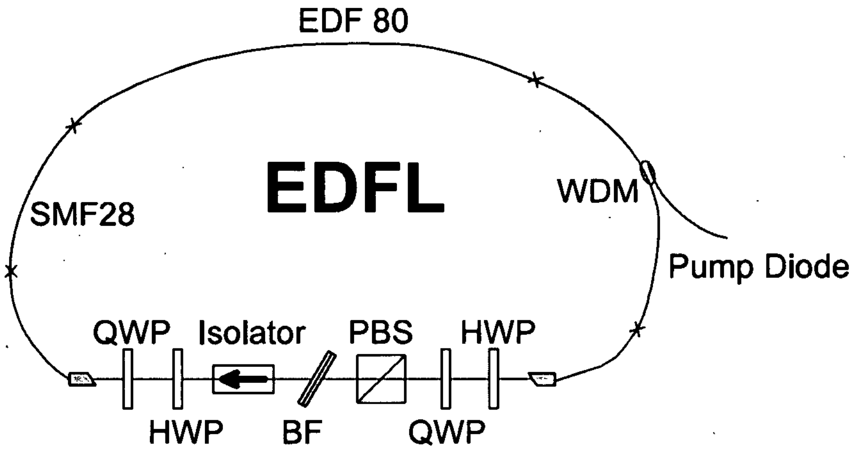

Figure 2.4: Experimental configuration of Er^{3+} doped fiber ring cavity laser. EDFL, erbium-doped fiber laser; EDF, erbium-doped fiber; SMF28, single mode fiber; WDM, wavelength division multiplexer; QWP, quarter-wave plate; HWP, half-wave plate; BF, birefringent filter; PBS, polarizing beam splitter.

lasers that operate in the soliton regime have inherent practical limits on their pulse width and pulse energy due to spectral sideband generation and saturation of the APM [18]. There is a tendency to enter multiple-pulse operation with increased pump power due to quantization of soliton pulses in a system with excessive gain. The product of the peak amplitude A_0 and the pulse width τ is fixed by the average dispersion and nonlinearity:

$$\text{soliton area} = A_0\tau = \sqrt{\frac{2\,|D|}{\delta}} \tag{2.1}$$

where D is the total group velocity dispersion (GVD), and δ is the SPM contribution of the Kerr medium.

in the non-soliton lasers, the lengths of large positive- and negative-dispersion fiber cause the pulses to be alternately stretched and compressed as they circulate in the cavity. Thus the average peak power in the laser is lowered significantly. As a result, the net nonlinear phase shift per pass is lower. The total cavity dispersion of this kind of configuration is slightly positive. Because the total dispersion in the cavity is oscillating back and forth from strongly positive to strongly negative, the pulse that is dumped may have a large chirp, which is, however, highly linear. Therefore, the chirp can then be compressed with an external dispersion delay line using either fiber, prisms or gratings as the compensation mechanism. As shown in Fig. 2.4, the stretched pulse, which has a width of $\sim$ 1 ps is dumped out from one output of the PBS. As discussed in Chapter 3, section 4.2 this pulse is compressed to $\sim$ 100 fs using a short piece of anomalous dispersion fiber.

When building the EDFL that I used in my experiment, we want the total cavity dispersion to be slightly positive and to oscillate between large positive and large negative so that the mode-locked fiber laser will operate in the non-soliton stretched-pulse regime. In the cavity of the EDFL, three types of fibers are used. They are single mode fiber (SMF-28), Corning Flexcor 1060 fiber and erbium-doped fiber. The GVDs of former two types can be calculated from the combination of their material and waveguide dispersion and also the Sellmeier equation [21] , which gives the refractive index n as a function of wavelength [3]. And the refractive index can be

[3]Some Sellmeier equations are also temperature-dependent.

related to the GVD by its definition:

$$\beta(\omega) = n(\omega)\frac{\omega}{c} = \beta_0 + \beta'(\omega - \omega_0) + \frac{1}{2}\beta''(\omega - \omega_0)^2 + \cdots \tag{2.2}$$

where $\beta(\omega)$ is the mode-propagation constant and expanded in a Taylor series about the frequency ω_0 at which the pulse spectrum is centered; β' and β'' are defined as the reciprocal of the group velocity v_g and 2^{nd} order GVD parameter, which is responsible for pulse broadening. β'' is usually given in units of ps^2/km. The 2^{nd} order GVD parameters of SMF-28 and Corning Flexor 1060 fiber at 1550 nm are $-22\,ps^2/km$ and $-6\,ps^2/km$ [22], respectively. The GVD of the erbium-doped fiber needs to be measured for every time a new piece of fiber is going to be used, because the variation of the core size and different amount of dopant from fiber to fiber will result in the the different value of the GVD parameters. Since we know the GVD parameters of the other two types of fiber, that of the erbium-doped fiber is able to be judged by measuring the total dispersion of the whole cavity. Ref. [23] gives a method to measure the total dispersion of the whole cavity by measuring the cavity round-trip time at different wavelengths. Given the length of a special medium l and the total cavity length L, the accumulated round-trip phase is

$$\Phi(\omega) = \frac{\omega}{c}\{L + [n(\omega) - 1]\} \tag{2.3}$$

where ω is the circular frequency at which the laser runs; c is the speed of light in vacuum; $n(\omega)$ is the frequency-dependent refractive index of the medium [4]. Now the group delay is simply defined as the frequency derivative of the round-trip phase,

$$T = \frac{\partial \Phi}{\partial \omega} = \frac{L-l}{c} + l\frac{\partial}{\partial \omega}\left[n(\omega)\frac{\omega}{c}\right] \tag{2.4}$$

However, the group velocity (or the β') is defined as

$$\frac{\partial}{\partial \omega}\left[\frac{n(\omega)\,\omega}{c}\right] = \frac{1}{v_g} = \beta' \tag{2.5}$$

therefore

$$T = \frac{L-l}{c} + l\beta' \tag{2.6}$$

The GVD parameter has been given in the Eq. 2.2 as the frequency derivative of the reciprocal of group velocity. So

$$\beta'' = \frac{\partial}{\partial \omega}\left(\frac{1}{v_g}\right) = -\frac{\lambda^2}{2\pi c}\frac{\partial}{\partial \lambda}\left(\frac{1}{v_g}\right) \tag{2.7}$$

Then by measuring the wavelength derivative of the cavity round-trip time, we directly obtain total dispersion:

$$\frac{\partial T}{\partial \lambda} = -\frac{2\pi c}{\lambda^2} l\beta'' \tag{2.8}$$

If the whole cavity consists of several types of media, the equation above will be rewritten as

$$\frac{\partial T}{\partial \lambda} = -\frac{2\pi c}{\lambda^2}\sum_{\mathrm{i}} l_{\mathrm{i}}\beta''_{\mathrm{i}} \tag{2.9}$$

The right-hand-side of Eq. 2.9 is the product of a constant $(2\pi c/\lambda^2)$[5] and

[4]There isn't a factor of 2 in the front of the $\Phi(\omega)$'s expression because of the ring cavity configuration of our laser.

[5]Although there is a small change of the central wavelength (λ) during the process of

the total dispersion of the cavity. The left-hand-side of Eq. 2.9 is the wavelength derivative of the round-trip time. Given there is a linear relationship between the round-trip time and the central wavelength, the wavelength derivative of the round-trip time is just the slope of the round-trip time versus central wavelength curve. Therefore, by measuring the round-trip time at different wavelengths and then linearly fitting the data, the wavelength derivative of the round-trip time (the right-hand-side of the Eq. 2.9) is obtained. Then the total dispersion of the whole cavity can be calculated from Eq. 2.9. In practice, we let the fiber laser run in a not very well mode-locking mode. In other words, the spectrum of the fiber laser is just several nanometers wide, which makes it easier to decide the central wavelength. By adjusting the wave-plates and birefringent filter in the cavity, the central wavelength is able to be changed in a range of 40 nm. The central wavelength is measured by the optical spectrum analyzer and the round-trip time is measured by the photodetector. The measured data and the fitted line is shown in Fig. 2.5 The calculated total dispersion from this curve is $(-1.9357 \pm 0.0060) \times 10^{-5}$ sec/m. We have known the GVD parameters of the SMF-28 and Corning Flexor 1060 fiber and the lengths of these two fiber and erbium-doped fiber, the GVD parameter of the erbium-doped fiber that we use is calculated to be $+61\ ps^2/km$.

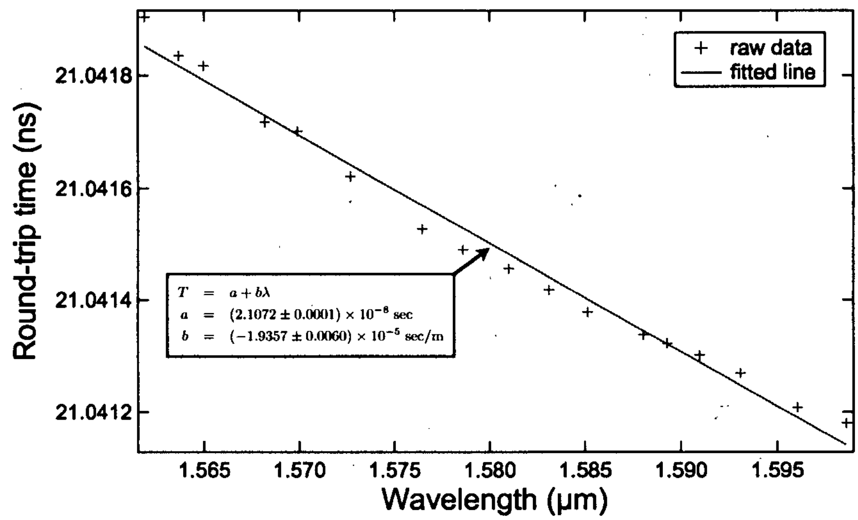

Figure 2.5: Round-trip time (T) of the EDFL vs. wavelength (λ) at which it runs in continuous-wave mode. Red crosses spot the measured data. The blue line gives the linearly fitted line. Its slope is the right hand side of the Eq. 2.9, which is proportional to the total dispersion of the whole cavity.

2.2 Femtosecond frequency combs

The frequency comb is not a new concept already. It is often used to measure the energy levels of different elements transitions. More than 20 years ago, the frequency comb of a mode-locked picosecond dye laser was first used as a ruler in the frequency domain to measure the $4d$ fine structure splitting of sodium [24]. The frequency comb is the representation of the output of mode-locked laser in the frequency domain. Generally, it is easier to comprehend the output, which is a train of pulses with regular intervals, in the time domain as shown in Fig. 2.6(a). The interval between two adjacent

measuring the total dispersion, it is still appropriate to use a constant number of 1550 nm for it.

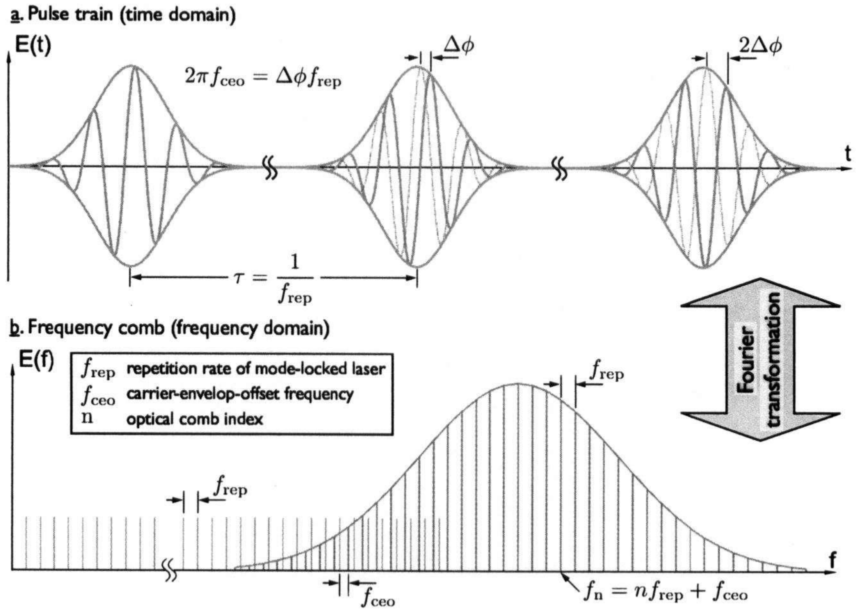

Figure 2.6: The representation of the ultrashort pulse in the time domain (pulse train) and frequency domain (frequency comb). In a, the green curve (Gaussian shape) is the envelope of the pulse trains and the red curve (oscillating curve) represents the carrier underneath the envelope. Due to the difference of the group velocity than the phase velocity, there is a phase shift of $\Delta\phi$ between them after each pulse. In frequency domain in b, it corresponds to the carrier-envelope-offset frequency f_{ceo}.

pulses τ is the period of the pulse train. $1/\tau$ is its repetition rate f_{rep}. The envelopes of pulses are drawn in green curve in Fig. 2.6(a). The underlying carrier with optical frequency, corresponding to the infrared light at 1550 nm in our case, is represented by the red curve. Due to the difference between the group velocity and the phase velocity in the cavity, there is a phase shift of $\Delta\phi$ between the carrier and envelope after every pulse. This phase shift is proportional to the carrier-envelope-offset frequency f_{ceo}, which is given in frequency domain in every frequency components' expression, $\nu_{\mathrm{n}} = nf_{\mathrm{rep}} + f_{\mathrm{ceo}}$.

The concept of femtosecond frequency combs is especially useful in the optical metrology, because narrower pulse corresponds to a wider spectrum. And a frequency spectrum extending over one octave is desired for realizing carrier-envelope phase control, which is one of the most important aspect for making direct absolute optical frequency measurements [25].

Although, in our experiment we don't have such rigorous demands on the width of the pulse, a narrow pulse is still wanted for two reasons. First, you will see the scheme 1 for remote synchronization in Chapter 3. The pulse will be spread by the grating and a photodiode will be used to receive the signal at each extreme of the spectrum. A bigger difference in optical frequencies between the signals received by two photodiodes is desired for getting a bigger nominal central frequency, which is inversely proportional to the timing jitter. Second, the total output power of the mode-locked fiber laser is merely ~ 50 mW, which will be split and shared by both the reference and transmission arm. Also because of the loss at many optical elements and optical fiber during the transmission process, the optical power of the pulse when it arrives the measuring setup is quite low and no more than 2 mW. A narrow pulse means a larger peak power, which could guarantee successful interferometric cross-correlation measurement of the timing jitter (see Chapter 5).

2.3 Remote synchronization techniques

2.3.1 Microwave and optical frequency distribution

There are varieties of methods for microwave and optical frequency transmission. Amplitude modulation (AM) and frequency modulation (FM) can be applied to transfer the rf standard through the global positioning system (GPS) [1] for example. Optical fiber can be used to transfer an optical frequency standard from the CW laser [26]. The advantages of the mode-locked laser for frequency transfer can be generally summarized in three points. First, it provides a method for simultaneously transmitting the optical and radio frequency references. As shown in Fig 2.6, the repetition rate of the transmitted pulse trains from the mode-locked laser (f_{rep}) represent a rf reference, while the positions of frequency comb lines from mode-locked laser represent an optical frequency reference ($\nu_{\mathrm{n}} = nf_{\mathrm{rep}} + f_{\mathrm{ceo}}$). Second, the transmitting laser can be directly stabilized to an optical frequency standard, even when using its radio frequency reference. Third, short pulses from the mode-locked laser provide a very sensitive way to measure and control timing jitter introduced during transmission by cross-correlation setup. This will be covered.

2.3.2 Previous experimental schemes and setups

As early as 1994, researchers in Colorado had used optical fiber to disseminate the optical frequency signal to a remote site with passive cancellation of noise [26]. The scheme that they used was to pre-modulate the phase of the input light beam to the fiber with the negative of the fiber noise so the beam can emerge from the far end noise-free relative to the laser source.

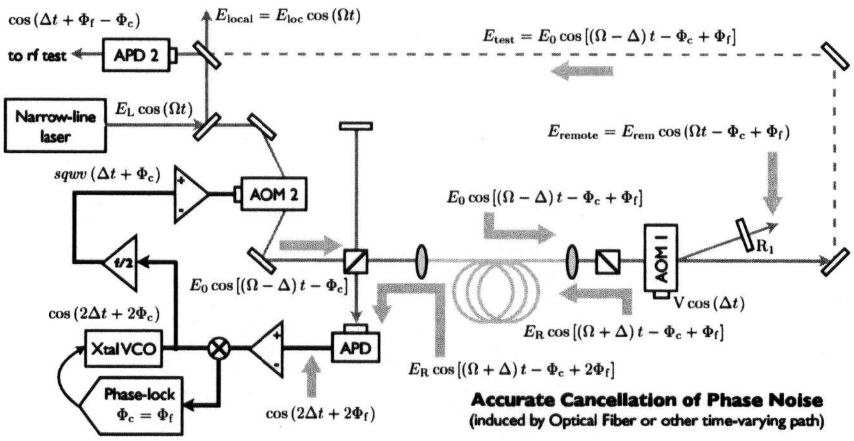

Figure 2.7: Frequency shifter AOM1 (acousto-optic modulator) at a remote site is double passed, so the frequency of the returned optical beam is offset by 2Δ. In this fiber-based example, one-way momentary phase induced by the fiber is Φ_f, becoming $2\Phi_f$ when the beam returns to the source end. The regenerated beat signal is $\cos(2\Delta t + 2\Phi_c)$, which is frequency/phase divided by 2 and filtered to be the driving source for the phase-noise compensator AOM2. With ideal phase locking, the correction phase Φ_c closely matches Φ_f, so noise cancellation is nearly perfect. Xtal VCO, voltage-controlled crystal oscillator.

The schematic setup is shown in Fig. 2.7. The 532 nm laser source is a frequency-doubled Nd:YAG non-planar ring oscillator. A 25 m jacketed fiber, which is designed to be polarization-maintaining, is used to show the fiber contribution to the noise in a realistic context. The 75 MHz AOM1 (acousto-optic modulator) is double passed with retro-reflecting beam splitter R_1 at the remote end. Thus twice of the fiber phase information appear as phase shifts on the 150 MHz beat note detected by the avalanche photodiode

(APD) at the source end. The reference signal shown as $\cos(2\Delta t + 2\Phi_f)$ in Fig. 2.7 is used by a precision phase-locking circuit that controls the phase of a voltage-controlled crystal oscillator. So its output phase $2\Phi_c$ is accurately equal to the fiber noise reference $2\Phi_c$. The oscillator's output is divided by 2 and bandpass filtered, amplified and sent to the AOM2, located at the source end, to precancel accurately the phase to be added on the light transmitted by the fiber. With the help of this setup shown in Fig 2.7, a mHz accuracy of the cancellation of fiber-induced degradation is achieved. Otherwise the bandwidth of the optical output of the CW laser would suffer a relative $\sim$ 100 Hz broadening.

In 2005, researchers transferred the pulse trains generated by the mode-locked fiber laser through several kilometers laboratory-based fiber link and got the rms timing jitter of 20 fs via passive noise cancellation over the bandwidth from 1 Hz to 100 kHz [7]. The setup used to measure and actively cancel the fiber transmission noise is shown in Fig. 2.8. The output of the free-running fiber laser is split into two portions. One portion provides the reference against which noise introduced by the transmission link is to be measured. The second portion is transmitted through the fiber-transmission link and an adjustable delay line. The reference and transmitted signal pulse trains are each detected on two photodetectors and then filtered to select the desired harmonic of the laser repetition frequency. The jitter introduced during transmission is measured by mixing the reference and transmitted signal at the 81st harmonic (7.84 GHz) in quadrature. The measured phase

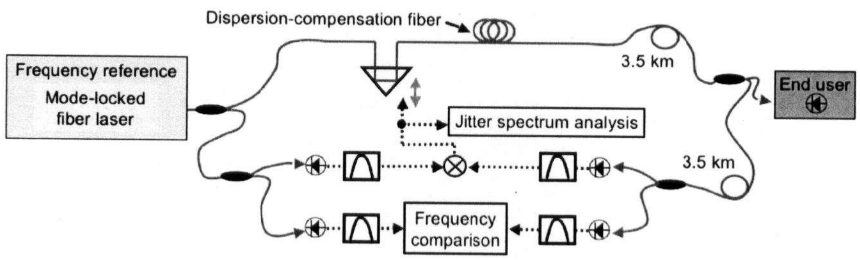

Figure 2.8: Schematic of the setup for detecting and stabilizing jitter introduced during the transfer of fiber-laser pulses. The single mode fiber is preceded by the DCF or the DSF. The signals from the upper pair of detectors are set in quadrature with the phase shifter and mixed to determine the phase noise of the transfer. The phase error is fed to the adjustable delay line for noise cancellation. The lower set of detectors is used for out-of-loop determination of the frequency instability of the transfer.

noise is fed back to the adjustable delay line to cancel the fiber noise. the other two signals are compared outside the locking loop at the 8^{th} harmonic (774 MHz).

To my knowledge, for transferring the optical frequency signal through optical fiber to the remote user, Ma's experiment [26] had canceled the 25-meter-fiber-induced degradation of a clean input with millihertz accuracy. The fiber-induced degradation would otherwise cause hundreds-of-hertz additional bandwidth. For transferring the radio frequency signal through optical fiber to the remote user, Holman's experiment in 2005 [7] reduces the timing jitter for transferring the signal through a 6.9-(4.5-) km round-trip fiber network to 37(20) fs over the bandwidth from 1 Hz to 100 kHz. Hudson's experiment in 2006 [27] has further reduced the timing jitter during transmitting via a 7 km fiber link to a level of 16 fs.

2.4 Standard measurement techniques of jitter

There are typically two classes of characterization of a frequency source [8],[28], which are used separately in different situations. The first involves measuring how much the fractional frequency fluctuations of the source signal vary as a function of the time over which the frequency is averaged and is expressed using Allan deviation [29]. It is often applied when characterizing the signals long-term stability. The second method for characterizing the frequency stability is to measure the phase noise, which represents how much the phase of the signal is jittering. This approach is often used when considering the signals' short-term stability.

2.4.1 Allan deviation

The Allan deviation [29], $\sigma_y(\tau)$, can be computed from a series of consecutive frequency measurements, each obtained by averaging over a period of time τ. This averaging time corresponds to the gate time of a frequency counter used to make the frequency measurements. In order to know how $\sigma_y(\tau)$ can be computed from these frequency measurements, it is necessary to introduce several definitions. The signal from the frequency source can be expressed as

$$V(t) = V_0 \cos[2\pi\nu_0 t + \phi(t)] \tag{2.10}$$

where V_0 is the amplitude of the signal, ν_0 is its nominal center frequency, and $\phi(t)$ represents time-varying deviations from the nominal phase $2\pi\nu_0 t$.

The instantaneous frequency is then given by

$$\nu(t) = \nu_0 + \frac{1}{2\pi}\frac{\mathrm{d}}{\mathrm{d}t}\phi(t) \tag{2.11}$$

and the instantaneous fractional frequency deviation from the nominal center frequency is given by

$$y(t) = \frac{1}{2\pi\nu_0}\frac{\mathrm{d}}{\mathrm{d}t}\phi(t) \tag{2.12}$$

The Allan deviation for an averaging time τ is then defined as

$$\sigma_y(\tau) \equiv \left\langle \frac{1}{2}[\bar{y}(t+\tau) - \bar{y}(t)]^2 \right\rangle^{1/2} \tag{2.13}$$

where $\langle\rangle$ indicates an infinite time average and $\bar{y}$ represents the time average of $y(t)$ over a period τ [30].

2.4.2 Phase noise spectral density

In practice, one of the methods for characterizing the synchronization stability is to measure the phase noise of the error signal which tells us how much the delay between two synchronized signals is jittering in phase [7],[28]. The phase noise is determined by measuring the phase fluctuation of a signal with respect the phase of the reference signal. If the frequency of the reference signal, the nominal central frequency of the measured signal is ν_0, and ϕ_0 is the arbitrary fixed phase of the reference, $\phi(t)$ represents the phase deviation of the measured signal from the $2\pi\nu_0 t$, then the reference signal is $\propto \cos[2\pi\nu_0 t + \phi_0]$ and the measured signal is $\propto \cos[2\pi\nu_0 t + \phi(t)]$. In order to get the phase difference term in the mixing product of these two signals. They are mixed together using a mixer and the required term is isolated with a low-pass filter (LPF), which will produce a signal that can be expressed as

$$A(t) = A_0 \cos\left[\phi(t) - \phi_0\right] \tag{2.14}$$

where A_0 is the amplitude of the mixer output and depends on the amplitudes of two mixed signals. Generally, a phase shifter will be used in the reference signal arm (see 3.2) to set $\phi_0 = \pi/2$, which simplify $A(t)$ to

$$A(t) = A_0 \sin\left[\phi(t)\right] \tag{2.15}$$

Typically, the phase deviations, $\Delta\phi$, of $\phi(t)$ from zero are sufficiently small to estimate the ratio of phase deviation to the amplitude deviation of the measured signal from zero by

$$\frac{\Delta\phi}{\Delta A} = \left(\left.\frac{\mathrm{d}A}{\mathrm{d}\phi}\right|_{\phi=0} \right)^{-1} = A_0^{-1} \tag{2.16}$$

The amplitude of the mixed signal, A_0, can be determined by tuning the phase shifter in the reference arm to adjust ϕ_0 from 0 to π and measuring the maximum and minimum output voltage level from the mixer. The difference between the max. and min. is the peak-to-peak value of the mixer output, namely twice of the amplitude. Then a Fourier transform is performed over the time domain measured signal, $A(t)$, to give the $\tilde{A}(\nu)$, which represents the root-mean-squared (rms) fluctuation of $A(t)$ about zero at each measured frequency component in a bandwidth of 1 Hz and has a unit of fs/$\sqrt{\text{Hz}}$. The amplitude density ($\tilde{A}(\nu)$) from the mixer could be determined by measuring through the fast Fourier transform (FFT) spectrum analyzer directly or transforming from the time signal from a digital oscilloscope (see the description in the Section 5.1.3 for the process of FFT on time signal).

2.4.3 Timing jitter

Intrinsically, phase noise and timing jitter are the same thing. For analyzing the remote transfer of a microwave frequency reference, it is common to express this as timing jitter, which will also be mainly used in this document. The quality of the remote transmission is often reported as the timing jitter integrated over a certain frequency range. The method of determination of the phase noise has been given in the previous section. The timing jitter is related to the phase noise through Eq. (2.17),

$$\delta\tilde{T}(\nu) = \frac{\delta\tilde{\phi}(\nu)}{2\pi\nu_0} = \frac{\tilde{A}(\nu)}{2\pi\nu_0 A_0}\left[\frac{\text{second}}{\text{Hz}^{1/2}}\right] \tag{2.17}$$

More specifically, the jitter spectral density $\delta\tilde{T}(\nu)$ of the error signal represents the rms timing jitter at each frequency in a 1 Hz measurement bandwidth and is proportional to the rms phase fluctuation $\delta\tilde{\phi}(\nu)$, where $\tilde{A}(\nu)$ is the measured error signal as a function of frequency, A_0 is the half peak of the unlocked sinusoidal error signal and ν_0 is the nominal center frequency of the reference and transmission signals. In order to calculate the total rms timing jitter (T_{rms}), $\delta\tilde{T}(\nu)$ is integrated over a frequency range,

$$T_{\text{rms}} = \sqrt{\int_{\nu_l}^{\nu_h}\left[\delta\tilde{T}(\nu)\right]^2 \mathrm{d}\nu}\,\left[\text{second}\right] \tag{2.18}$$

where ν_l and ν_h are the integration lower limit and higher limit, which are determined by the specific application for which the frequency reference is being transferred.

2.4.4 Intensity cross correlation: non-collinear approach

In a specific situation where the pulse trains from two mode-locked fiber lasers or from the same mode-locked fiber laser where one is used as a reference signal locally and the other is transmitted to the remote location for some specific application and retro-reflected back to be synchronized, an alternative all-optical method for detecting the timing jitter between the two pulse trains (or two optical frequency combs) is available [31, 32, 33, 34].

This approach uses the similar setup for measuring the pulse width by the intensity auto-correlation (IAC). It involves measuring the cross-correlation signal between the two pulse trains by overlapping the pulse trains temporally and spatially in a nonlinear crystal and detecting the sum-frequency generation. It is common to arrange the two pulse trains crossing through the nonlinear crystal non-collinearly and receiving the sum-frequency generation by a photo-multiplier tube (PMT) in a direction different from the incident direction of either pulse train as shown in Fig. 2.9. Once the repetition rates of the two pulse trains are locked, adjusting the time offset between them to overlap them at nearly the half maximum of the intensity level will give the maximum slope point on the curve of the signal. That results in the most sensitive measurements of the timing jitter possible by taking the product of the slope and the voltage fluctuation of the intensity

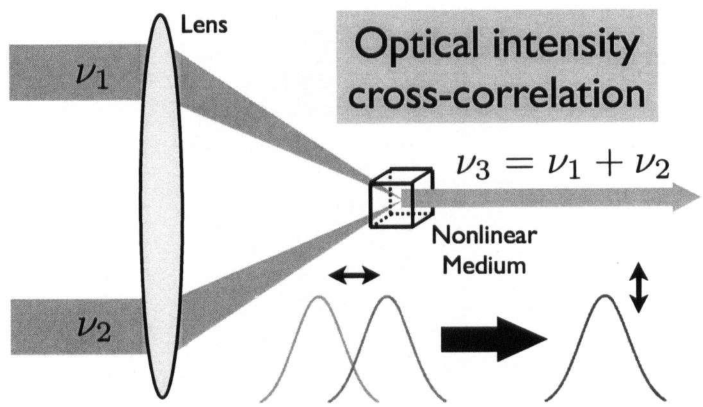

Figure 2.9: Schematic setup for the timing jitter measurement by intensity cross-correlation. Two beams with optical frequency of ν_1 and ν_2 are focused non-collinearly onto a nonlinear crystal. The 3rd beam with the frequency of $\nu_3 = \nu_1 + \nu_2$ is generated through sum-frequency generation (SFG) in a direction other than that of the two input beams. Given two input signal are two pulse trains, by measuring the intensity fluctuation of the SFG signal, the timing jitter between two input pulse trains is able to be calculated. The maximum sensitive measurement is obtained when two input pulses are adjusted to overlap at half-maximum position.

cross-correlation signal at that point. This is a very sensitive approach for measuring the timing jitter given a $\sim 10-100$ fs pulse width and unchirped pulse. It is better than the microwave detection approach by mixing the harmonics of repetition rates of two pulse trains which is discussed in the section 2.3.2, because intensity cross-correlation is an independent and out-of-loop measurement and exempt from the extra noise introduced in by the phase shifter, the free-space photodiodes for detecting the repetition rates, the mixer and the rf amplifiers which are necessary for amplifying the signals to the required level by the mixer and PZT driver.

Although the intensity cross-correlation approach is very good at measuring the timing jitter, the collinear interferometric cross-correlation approach provides an even better sensitivity. This will be discussed in Chapter 5.

Chapter 3

All-optical synchronization by spectral leveraging

This chapter explains our scheme 1 (spectral leveraging technique) for actively canceling the noise induced during transmitting the pulse trains through the optical fiber link. The physics underneath this technique, the experimental setup and the measured in-loop jitter after active cancellation are described in sequence.

3.1 Spectral leveraging technique (scheme 1)

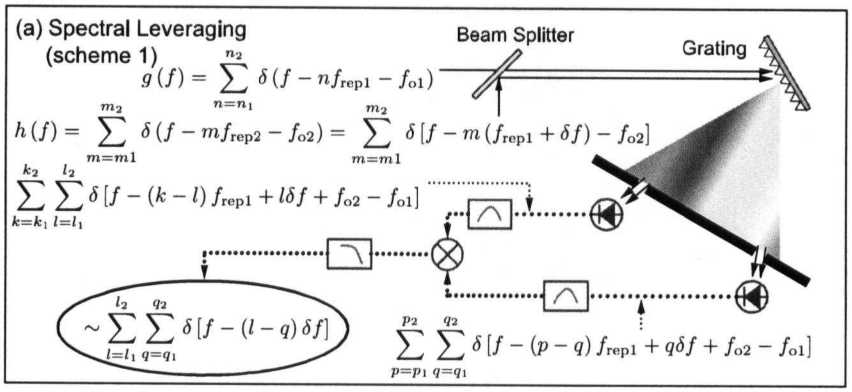

Figure 3.1: All-optical generation of an error signal for synchronization of two pulse trains (or two fs frequency combs). When the combs are close in repetition rate, we can express one (the slave) as having a slight amount of frequency noise on its repetition rate (δf) as compared to the master comb. In this figure we denote the optical and detected electrical frequencies as delta functions. In spectral leveraging (Scheme 1), the master and slave combs are combined collinearly and then resolved at two extremes of the spectrum. After detection the indices (k, l, p and q) represent the respective detection optical bandwidths of the two combs. By filtering the resulting heterodyne beat signal at a harmonic of the f_{rep1} and mixing the result, the dependence on the different in offset frequencies (f_{o1} and f_{o2}) is eliminated and a spectrally leveraged error is produced.

In chapter 1 we have briefly introduced our new approach to all-optical synchronization. This method is best described in the frequency domain where fs pulse trains can be described as frequency combs [35]. The two fs pulse trains that are to be synchronized are combined collinearly and then spectrally resolved. The resulting frequencies as detected by the photodiodes are shown in Fig. 3.1(a) where the indices k & l (p & q) represent the summation of the respective combs over the optical detection bandwidth of the red (blue) side of the combined spectra. The optical heterodyne beat between the two pulse trains produces a set of harmonics spaced by f_{rep1} in the rf domain along with "noise" sidebands on these harmonics. As indicated in Fig. 3.1, it is these sidebands that contain the optically leveraged error signals. To access these signals, each heterodyne beat is filtered at f_{rep1} (or a harmonic thereof) and then mixed together. The result is an error signal is produced that is proportional to the comb spacing difference between the two lasers (δf_{n}) times the spectral separation between the two optical beats. This spectral leveraging technique is denoted as scheme 1. As the difference between the indices k and p can be as high as $\sim 10^5$ for reasonable separation ($\sim$ 50 nm), a corresponding 10^5 increase in sensitivity of the error signal is realized. This approach is similar in motivation to using a high microwave harmonic (such as the 100^{th}) when individually detecting each pulse train for conventional synchronization [32]. In this case we are effectively detecting at the $\sim 10^5$ harmonic. Another key point is that by taking the difference between the two heterodyne beats, the generated error signal is independent of the offset frequencies of each comb. An advantage this approach has over any time-domain based correlation technique is that perfect chirp compensation is not necessary as the error signal is not derived from the cross-correlation overall envelope. However, it is helpful to match the chirp (as close as possible) in the two signals as this enables more comb lines to simultaneously contribute to the overall error signal thereby increasing its signal to noise.

In the previous paragraph, we discussed the principle of the spectral leveraging scheme for error signal generation in the simplified expressions. Next we will talk about it in the full mathematical expressions and still in the frequency domain. The electrical field of each pulse train could be represented in the complex format in the frequency domain as

$$\tilde{E} = \sum_{m=m_1}^{m_2} A_{\mathrm{m}} \exp\left[i\left(m f_{\mathrm{rep}} + f_{\mathrm{ceo}}\right)\right] \tag{3.1}$$

where the index of the combs of the spectrum ranges from m_1 to m_2, A_{m} is the amplitude of the corresponding frequency component; f_{rep} is the repetition frequency of the pulse train and f_{ceo} is the offset frequency.

Let's focus on the red side of both spectra and just consider the five consecutive frequency combs of each spectrum. The summation of them is given by,

$$\tilde{E}_{\mathrm{k}} = A_{\mathrm{k}} \sum_{m=k}^{k+5} \exp\left[i\left(m f_{\mathrm{rep1}} + f_{o1}\right)\right] \tag{3.2}$$

This is the expression for one of the pulse trains, where we assume that every frequency component has the same amplitude A_{k}. For the other one, we substitute the subscript k, rep1 and o1 with l, rep2 and o2, respectively.

Due to the noise during transporting to the remote site in optical fiber, the transmitted pulse train has the slightly different repetition rate and offset frequency. The two pulse trains interfere with each other optically before they are detected by the photodiode. The intensity of the interference signal can be expressed as

$$\begin{aligned} I_{\mathrm{c}} &= \left(\tilde{E}_{\mathrm{k}}^{*}+\tilde{E}_{\mathrm{l}}^{*}\right)\left(\tilde{E}_{\mathrm{k}}+\tilde{E}_{\mathrm{l}}\right) \\ & 2\left[2C_1^2A_{\mathrm{k}}^2+C_2A_{\mathrm{k}}A_{\mathrm{l}}+2C_3^2A_{\mathrm{l}}^2\right] \end{aligned} \tag{3.3}$$

where * represents the complex conjugate, C_1, C_2 and C_3 are defined as

$$C_1 = \cos\left(\frac{f_{\mathrm{rep1}}t}{2}\right)+\cos\left(\frac{3f_{\mathrm{rep1}}t}{2}\right)+\cos\left(\frac{5f_{\mathrm{rep1}}t}{2}\right) \tag{3.4a}$$

$$C_2 = \sum_{\alpha=0}^{5}\sum_{\beta=0}^{5}\cos\left\{\left[(k+\alpha)\,f_{\mathrm{rep1}}-(l+\beta)\,f_{\mathrm{rep2}}+(f_{\mathrm{o1}}-f_{\mathrm{o2}})\right]t\right\} \tag{3.4b}$$

$$C_3 = \cos\left(\frac{f_{\mathrm{rep2}}t}{2}\right)+\cos\left(\frac{3f_{\mathrm{rep2}}t}{2}\right)+\cos\left(\frac{5f_{\mathrm{rep2}}t}{2}\right) \tag{3.4c}$$

The coefficient of the cross term in Eq. (3.3) contains the repetition rate difference between the reference and the transmitted pulse trains. The repetition rate of the transmitted pulse train (f_{rep1}) is able to be expressed as having a slight amount of frequency noise (δf_{n}) as compared to the repetition rate of the reference pulse train (f_{rep2}), namely $f_{\mathrm{rep2}} = f_{\mathrm{rep1}} + \delta f_{\mathrm{n}}$. So the Eq. (3.4b) can be rewritten as

$$C_2 = \sum_{\alpha=0}^{5}\sum_{\beta=0}^{5}\cos\left\{\left[(k+\alpha-l-\beta)\,f_{\mathrm{rep1}}-(l+\beta)\,\delta f_{\mathrm{n}}+(f_{\mathrm{o1}}-f_{\mathrm{o2}})\right]t\right\} \tag{3.5}$$

The phase of each cos term is a product of time and frequency term. Every frequency term is a sum of a integer multiple of f_{rep1}, a integer multiple of frequency noise and a offset frequency difference. The Eq. (3.5) is derived for the red side of the interference signal. For the blue side, there is a similar expression, which is given in Eq. 3.6,

$$C_2 = \sum_{\alpha=0}^{5}\sum_{\beta=0}^{5} \cos\left\{\left[(p+\alpha-q-\beta)\, f_{\text{rep1}} - (q+\beta)\,\delta f_{\text{n}} + (f_{\text{o1}} - f_{\text{o2}})\right] t\right\} \tag{3.6}$$

In Eq. (3.5), the coefficient $(k+\alpha-l-\beta)$ is a very small positive integer, because $0 \leq \alpha$, $\beta \geq 5$ and k and l are the indices corresponding to the same frequency part in their own combs. When mixing the red and blue side optical heterodyne signal together, the f_{rep1} term and difference of the offset frequencies term are cancelled out between two sides. Only the frequency noise term, which is multiplied by the coefficient of $l-p$ of $120,000$, survives. So through the spectral leveraging approach, the frequency noise is amplified by a factor of 10^5.

3.2 experimental setup for spectral leveraging measurement

We have experimentally demonstrated the all-optical error signal generation with spectral leveraging technique by detecting and canceling the noise added when a pulse train from a mode-locked fiber laser is propagated through a round-trip ~ 60-m fiber link. The specific setup of the spectral leveraging approach (scheme 1) is shown in Fig. 3.2. The rejection port (chirped) output from an mode-locked erbium-doped fiber laser [18] is

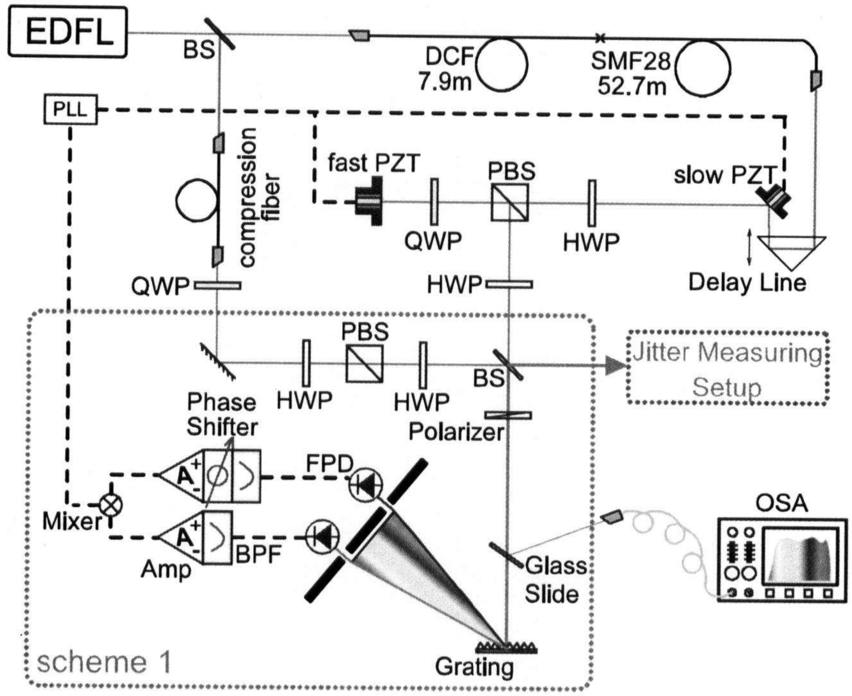

Figure 3.2: Experimental setup of optical heterodyne jitter cancellation with the optical heterodyne detection at two spectral extremes (Scheme 1). EDFL, mode-locked Erbium-doped fiber laser; BS, beam splitter; DCF, dispersion compensating fiber; SMF-28, single mode fiber; PZT, piezo-electric transducer; PBS, polarizing beam splitter; HWP, half-wave plate; QWP, quarter-wave plate; FPD, free-space photodiode; BPF, band-pass filter; Amp, radio frequency amplifier; OSA, optical spectrum analyzer; PLL, phase-locked loop.

split into two paths by a 50/50 non-polarizing broadband plate beamsplitter coated for 1100 – 1600 nm. One portion is saved for the reference signal and passed through a 83 cm of SMF-28 fiber to produce a compressed pulse width of 154 fs at full-width half-maximum (FWHM). The other portion is pre-compensated with 7.9 m of dispersion compensating fiber (DCF) before being launched into a 52 m spool of standard telecom fiber.[6] In this case the resulting pulse-width is 197 fs with an accompanying single pre-pulse with an intensity of 42% of the main pulse that is typical of uncompensated third-order dispersion [36]. The reason why we launch the pulse through the DCF fiber first and then through the standard telecom fiber is that the output of the EDFL is positively chirped and the SMF-28 fiber has the negative dispersion while DCF fiber has the positive dispersion. So if SMF-28 fiber is located in front of DCF fiber, the pulse will pass the soliton point (zero chirp), and the resulting strong non-linear effect due to the high peak power of the pulse will make the resulting chirp highly non-linear and difficult to compensate. The compressed reference pulse passes through a quarter-wave plate (QWP) and a half-wave plate (HWP), which are adjusted to maximize transmission through the PBS. The PBS works as a polarizer which linearly polarizes the reference pulse train. In the other arm, the re-compressed transmitted pulse coming out of 60-m link is reflected by a delay line first. The delay line is a right angle prism sitting on the translating stage and can adjust the optical length of the transmission arm by up to several centimeters in order to make the difference between the optical lengths of reference and transmission arms to be an integer multiple of the distance between two consecutive pulses in the train. After the light is reflected off at an angle of

[6]In an actual implementation of remote synchronization, a portion of the delivered signal would be retro-reflected back and compared with the reference signal. The noise during a one-way transit is assumed to be equal to twice the round-trip and the error signal is simply divided by 2. For experimental convenience we stabilized the round-trip signal, which is equivalent to a remote transfer of 30-m.

45° by a piezoelectric transducer (PZT), HWP is used to rotate the polarization of the pulse train to increase the transmission rate at the next PBS as much as possible. The horizontally polarized component of the pulse train will be transmitted through the PBS and will be reflected back by the fast PZT. The pulse train will pass back and forth through the QWP a total of two times, resulting in a 90° rotation of the polarization. So the originally horizontally polarized pulse train will become polarized vertically and will be reflected in the other direction when it comes back to the PBS again. Right now, the reference and transmitted signals are polarizing orthogonally. Both the reference and transmitted pulse trains were compressed in an effort to match their relative chirp and increase the overall signal-to-noise ratio. These two signals are then collinearly combined [37] and then passed through a 50/50 beam splitter (BS). One output of the beam splitter is used for measurement of the jitter (discussed in the chapter 5). The second output is passed through a polarizer to get the polarizing components of two arm's signal in the same direction and then reflected off a grating (600 lines/mm) and the optical heterodyne beat is detected at 1523 nm and 1573 nm with a bandwidth of $\sim$ 1.8 nm at each spectral extreme (see Fig. 3.3). For scheme 1 the spectral separation was 50 nm. With this spectral separation ($\sim$ 6 THz) and the repetition rate of the lasers (50 MHz), our implementation generates an error signal that is a weighted sum centered at approximately the $125,000^{\text{th}}$ harmonic. Each heterodyne beat is filtered at the third harmonic and then mixed together to produce the spectral leveraged error signal for synchronization. A phase-locked loop (PLL) is then utilized to pre-cancel the noise by actuating two free-space PZTs. The slow one (see the setup in Fig. 3.2) with 45°-incidence is in charge of the low frequency noise from dc to $\sim$ 300 Hz and has a long dynamic range of 9.1 ± 1.5 μm. The fast one (see the setup in Fig. 3.2) is responsible for the high frequency noise with a relative short dynamic range. To obtain the high frequency response the fast PZT is glued by two component Torr Seal onto a copper cylinder with a aluminum core and then mounted on to a heavy stage.

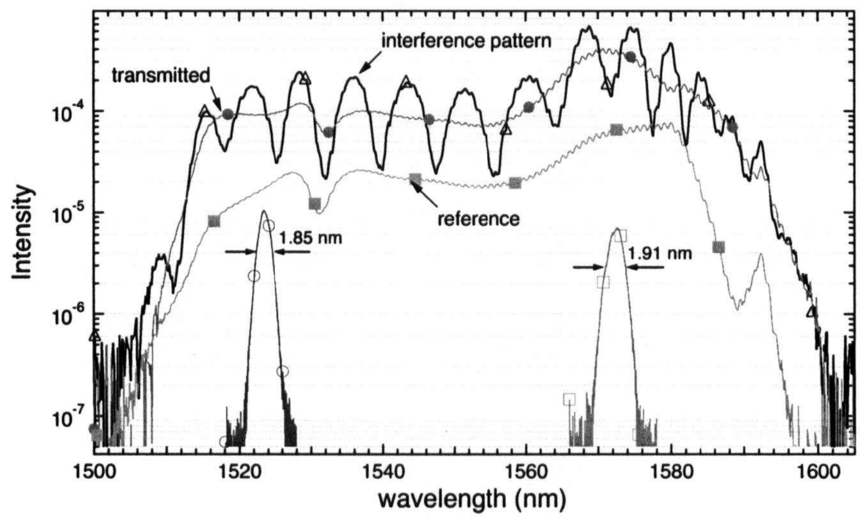

Figure 3.3: The green (with filled square) and purple (with filled circle) curves show the spectra of reference and transmission paths, respectively. The self-phase modulation due to transmission through $\sim$ 60-m fiber results in the slightly wider spectrum in the transmission arm with respect to the reference arm. The blue (with open circle) and red (with open square) curves are the spectra of the received signals at two spectral extremes. Each spectral slice has a bandwidth of $\sim$ 1.8 nm. The black curve (with open triangle) is the stable interference pattern of combined signal when PLL is activated.

Fig. 3.3 shows the pulses' spectra of the reference and transmission paths, the received signals at each spectral extreme and a stable interference pattern of the combined signal (when the PLL is activated for scheme 1). The high frequency interference fringes on all of the traces are due to Fabry-Perot effects within a glass slide (which wasn't anti-reflection coated) used to sample the various signals.

3.3 In-loop jitter measurement for scheme 1

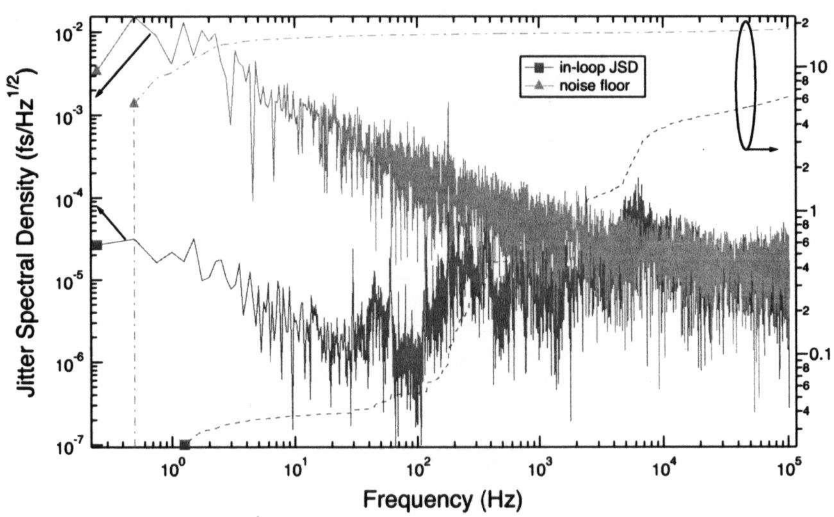

Figure 3.4: In-loop measurement of jitter spectral density (filled square and solid curve referring to left axis) and integrated jitter (filled square and dashed curves referring to right axis) of noise when actively canceled by the approach of spectral leveraging (scheme 1). The noise floor of the setup for this technique is also given (JSD in filled triangle and solid curve referring to left axis while integrated jitter in filled triangle and dashed curve referring to right axis).

The stable interference pattern of the combined signal shown in Fig. 3.3

indicates that the transmitted pulse train is stable with respect to the reference pulse train, but it is not possible to quantify the synchronization quality. So the integrated timing jitter, which is explained in the Section 2.4.3, is measured by the in-loop measuring setup for characterizing the synchronization stability. The in-loop means the signal used to synchronize the transmitted signal to the reference one is also applied to characterize the synchronization stability. So voltage signal straight out of the mixer (see the setup in Fig. 3.2) is split into two. One is sent to the PLL for actuating the PZTs to realize the synchronization, while the other is used by the FFT spectrum analyzer to measure the power spectral density. In fact, we use the amplified input monitor signal from the PLL since the output of the mixer is too weak to make an accurate enough measurement.

In our case measuring the in-loop jitter via the error signal is not straight forward. For the spectral leveraging scheme (scheme 1), the error signal contains many different terms (of the weighted sum of $k - p$, reference to Fig. 3.1), each with its own nominal central carrier frequency (ν_0 in Eq. (2.17)). In the worst case, the estimate of the nominal central carrier frequency is made using the minimum spectrum separation of 48 nm (reference to Fig. 3.3) between the two signals received individually at their own slit (blue and red side, see Fig. 3.2) to make $\nu_0 = 5.99$ THz. Using this value as the overall central frequency and following the prescription of Eq. (2.17), an integrated in-loop timing jitter, integrated over the bandwidth from 0.25 Hz to 102.4 kHz, of 6.2 as is measured. Since the jitter spectral density (JSD) curve shown in the Fig. 3.4 levels out at 10^5 Hz, it is reasonable to use the JSD value of 1.069×10^{-5} fs/Hz$^{1/2}$ at this point to estimate the JSD value between 10^5 Hz and 10^7 Hz. Thus the in-loop jitter, integrated from 0.25 Hz to 10 MHz, is 38 as. When doing this measurement, are always spikes at the integer multiples of 60 Hz, which could be either the intrinsic noise of the FFT spectrum analyzer itself or the AC power noise from the photodiodes, the amplifiers or the FFT spectrum analyzer. The JSD curve shown in Fig. 3.4 has been corrected by omitting those spikes.

Although the number given by the in-loop measurement looks good, it has some intrinsic disadvantages. The most serious one is the extra electrical noise introduced in by the amplifiers and the photosensors. But the influence of the extra noise to the in-loop jitter in our experiment is not as much as in Holman's experiment in 2005 [7] due to the huge amplification ratio of the error noise. In my experiment, the transmission noise is optically amplified through the interference between two pulse trains before being detected by the photodiodes. It is equivalent to measuring at the $120,000^{\text{th}}$ harmonic (5.99 THz/49.25 MHz) without amplifying the extra electrical noise.[7] So the effect of the electrical noise is weakened by a factor of 120,000. That is why we obtain a much smaller in-loop jitter than Holman's work in 2005. In other words, in previous work the actual transmission jitter was overestimated due to the measurement technique itself. Even though the in-loop jitter had been very small, the fact that the measured JSD curve has a bowl-shape and is

[7] In Holman's work in 2005, the error signal for the phase-locked loop is generated by mixing the 81^{st} harmonics of the repetition rates.

below the noise floor curve urges us to make an out-of-loop measurement to get a true measurement of the jitter. A totally new all-optical measurement approach will be discussed in Chapter 5 capable of performing this out-of-loop measurement.

Chapter 4

All-optical synchronization by optical heterodyne

This explains our scheme 2 (simple optical heterodyne) for actively canceling the noise induced during transmitting the pulse trains through the optical fiber link in this chapter. The physics underneath this technique, the experimental setup and the measured in-loop jitter after active cancellation are described in sequence.

4.1 Simple optical heterodyne technique (scheme 2)

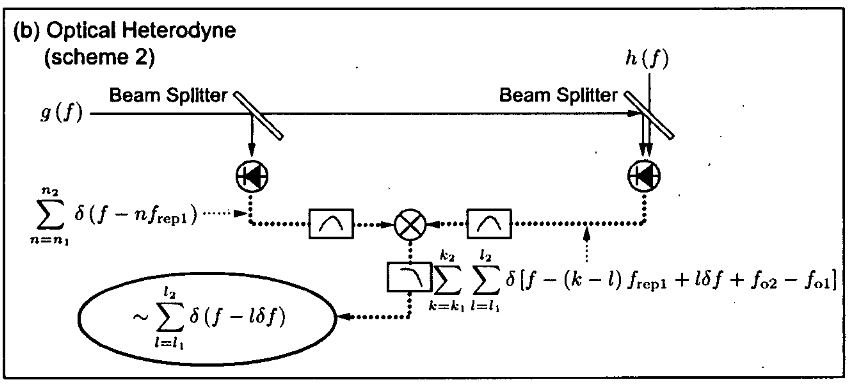

Figure 4.1: All-optical generation of an error signal for synchronization of two pulse trains (or two fs frequency combs). When the combs are close in repetition rate, we can express on (the slave) as having a light amount of frequency noise on its repetition rate (δf_{n}) as compared to the master comb. If the offset frequencies ($f_{\text{o1}} = f_{\text{o2}}$) are approximated as equal (see text for discussion of this approximation), then a simple optical heterodyne will also produce a leveraged error signal. The heterodyne beat is mixed with f_{rep1} to avoid noise present in the photo-detection process around DC to generate the error signal.

A slightly simpler approach is shown in Fig. 4.1 where an optical heterodyne is measured between the two combs. As before, the goal is to lock f_{rep1}

to f_{rep2}. This scheme relies on the fact that the combs' offset frequencies are equal ($f_{o1} = f_{o2}$) which isn't necessary true. In the application of delivery of stabilized frequency standards to remote locations, the transmitted and reference combs will have the same offset frequencies as long as there is not a rapid, time-varying change in the dispersion of the fiber link –such a condition will cause $f_{o1} \neq f_{o2}$ even though both combs are generated from the same laser. In our experimental setup the time-rate of change of the fiber link dispersion will not be an issue. Hence $f_{o1} = f_{o2}$ is satisfied and this technique will also produce a spectrally-leveraged error signal. In our implementation, the rf beat produced by the optical heterodyne is mixed with a harmonic of the f_{rep1} to avoid low frequency noise in the photo-detection process.

4.2 experimental setup for optical heterodyne measurement

In the optical heterodyne approach (denoted scheme 2), the experimental setup just needs to be slightly modified. The collinear signals (one output of the 2^{nd} beamsplitter) are directed toward a single photodetector. As indicated in Fig. 4.1, to generate the high-sensitivity error signal, the resulting optical heterodyne beat is mixed with a microwave signal f_{rep1} from the reference to avoid noise near DC. Then, similar to scheme 1, with this error signal a PLL is used to pre-cancel the noise. In fact, the setup for scheme 2 can be easily changed to the one for synchronizing the transmitted signal

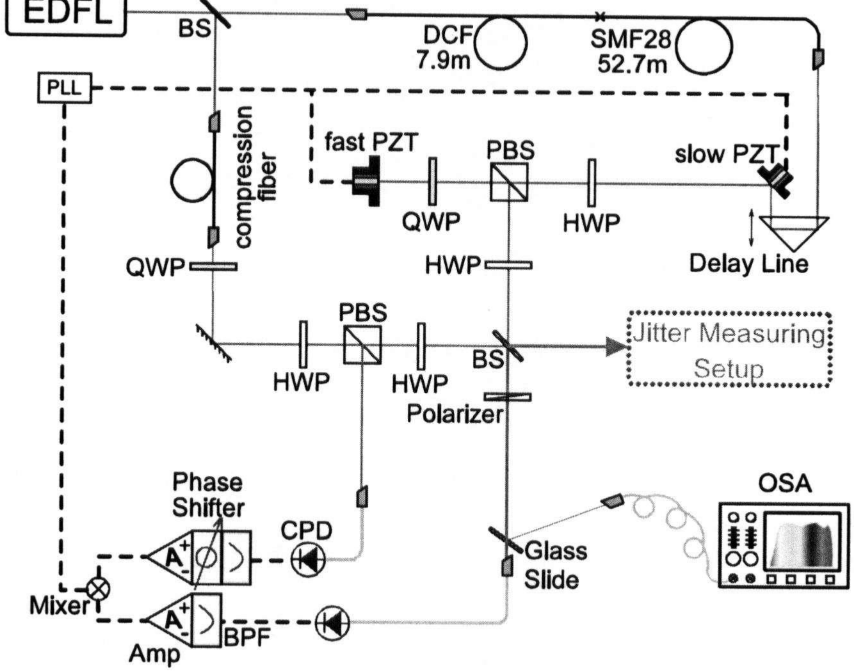

Figure 4.2: Experimental setup of optical heterodyne jitter cancellation with single optical heterodyne (scheme 2). EDFL, mode-locked Erbium-doped fiber laser; BS, beam splitter; DCF, dispersion compensating fiber; SMF-28, single mode fiber; PZT, piezoelectric transducer; PBS, polarizing beam splitter; HWP, half-wave plate; QWP, quarter-wave plate; CPD, fiber-coupled photodiode; BPF, band-pass filter; Amp, radio frequency amplifier; OSA, optical spectrum analyzer; PLL, phase-locked loop.

to the reference signal by measuring at the high harmonic of the repetition rate shown in ref. [7] by lining up the polarizer with the polarization direction of the transmitted signal rather than at 45 degree to that. We did the microwave measurement by this setup and the result is compared to the optical measurement and discussed in section 5.2.3.

4.3 In-loop jitter measurement for scheme 2

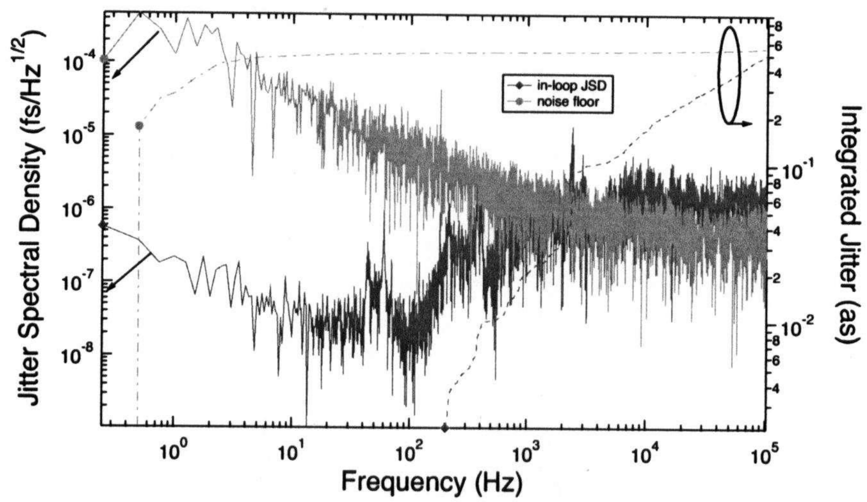

Figure 4.3: In-loop jitter measurement of jitter spectral density (filled diamond and solid curve referring to left axis) and integrated jitter (filled diamond dashed curves referring to right axis) of noise when actively canceled by the approach of simple optical heterodyne (scheme 2). The noise floor of the setup for this technique is also given (JSD in filled circle and solid curve referring to left axis while integrated jitter in filled circle and dashed curve referring to right axis).

Similar to what has been done for the spectral leveraging approach (scheme 1), the in-loop jitter, which has been described in the section 3.3, is also measured for simple optical heterodyne approach (scheme 2). The error signal contains many different terms (of the weighted sum of k, reference to Fig. 4.1), each with its own nominal central carrier frequency (ν_0 in Eq. (2.17)). In the worst case, the estimate of the nominal central carrier frequency is made using the minimum wavelength of the pulses' spectrum of 1530 nm (reference to Fig. 3.3) to make $\nu_0 = 195.9$ THz. Using this value as the overall central frequency and following the prescription of Eq. (2.17), an integrated in-loop timing jitter, integrated over the bandwidth from 0.25 Hz to 102.4 kHz, of 0.507 as is measured. Since the JSD curve shown in the Fig. 4.3 has come to be flat at 10^5 Hz, it is reasonable to use the JSD value of 9.0315×10^{-7} fs/Hz$^{1/2}$ at this point to estimate the JSD value between 10^5 Hz and 10^7 Hz. Thus the in-loop jitter, integrated from 0.25 Hz to 10 MHz, is 4.2 as. The background noise spikes at the integer multiples of 60 Hz are removed.

Chapter 5

Out-of-loop jitter measurement

In the chapters 3 and 4, the in-loop measurement of the transmitted timing jitter when reduced by the spectral leveraging (scheme 1) and simple optical heterodyne (scheme 2) are reported. However, the phenomena shown in Fig. 3.4 and Fig. 4.3 that the curves of noise floor are even higher than that of the measured in-loop jitter tells us that we should turn to a totally separated out-of-loop jitter measurement for a credible measuring of the noise performance. In my experiment, an all-optical out-of-loop jitter measuring setup, using APD for interferometric cross-correlation (ICC), is used. This chapter will describe this technique and its advantage. The results for jitter measurement in scheme 1 & 2 are also given.

5.1 All-optical timing jitter measurement: collinear approach

There are several methods for measuring the timing jitter when synchronizing two signals.

- *In-loop measurement at high harmonic of repetition rate*

  This method has been shown in the section 3.3 and the section 3.3. The error signal is obtained by mixing the reference signal and the measured signal at a high harmonic of the repetition rate. The measurement setup shares the same error signal with the feedback loop, which is used to control the PZTs within the transmission path to actively cancel the phase noise. However, the unavoidable electronic noise from the rf amplifier and the the mixer is a big problem. In addition, due to the existence of the electronic noise, the error signal sent to the PLL has the contributions from both the phase noise induced during transmission and the electronic noise from the electric component (i.e. rf amplifier, mixer). Therefore, the measured phase noise actually shows the phase fluctuation of the combination of these two processes. Especially, in case the electronic noise is strong enough to be comparable with the transmission phase noise, the interference between these two noises could make the measured phase spectral density even lower than the noise floor at low frequency range (see Fig. 3.4 and Fig.4.3).

- *Out-of-loop measurement at high harmonic of repetition rate*

  The only difference of this method from the previous one is a separate set of detectors and required electric components is used for determination of the frequency instability of the transfer, which means the out-of-loop. Although, the second problem mentioned above is solved, the electronic noise still keeps the noise floor at a high level and it is not possible to do an accurate phase noise measurement. The schematic setup for this method is shown in Fig. 2.8.

- *Out-of-loop measurement using intensity cross-correlation*

  This method has been introduced in the section 2.4.4. Because the intensity of the intensity cross-correlation signal is a function of the time-delay between the two input pulses. Therefore, by monitoring the intensity fluctuation of the intensity cross-correlation signal, the timing jitter between two pulses is able to be estimated. This method is absolutely out-of-loop, all-optical and with high resolution.

- *Out-of-loop measurement using interferometric cross-correlation*

  This method shares the same physics with the intensity cross-correlation method for monitoring the timing jitter. It is also out-of-loop, all-optical, but with even higher resolution. Another advantage of this method has over any time-domain based correlation method is that perfect chirp compensation is not necessary as the error signal is not derived from the cross-correlation overall envelope. However the dynamic range of this measurement technique is limited by the optical period (in my case 5.17 fs, the optical period of 1550 nm light). This method is going to be described in detail in the consecutive section.

An independent, out-of-loop measurement of the jitter was made to confirm this performance by an optical cross-correlation between the reference and transmitted pulse trains. Before reporting my special experimental configuration and results, let's spend several sections to give a background introduction on the interferometric cross-correlation (ICC), using two photon absorption (TPA) in Si-APD and how to convert time domain measurement to jitter spectral density by using FFT.

5.1.1 Interferometric cross-correlation (ICC)

In section 2.4.4, the intensity (non-collinear) cross-correlation [32, 38] has been introduced as a sensitive method for measuring the timing jitter between two pulse trains, which are generated from mode-locked lasers. However, the interferometric (collinear) cross-correlation measurement can provide an even higher degree of sensitivity.

In intensity cross-correlation (non-collinear), taking the sum-frequency generation realized by using the nonlinear crystal and PMT as an example, the measured sum-frequency signal has the profile which is given by

$$A_{\mathrm{c}}(\tau) = \int_{-\infty}^{+\infty} I_{\mathrm{t}}(t)\, I_{\mathrm{r}}(t-\tau)\, \mathrm{d}t \tag{5.1}$$

where $I_{\mathrm{t}}(t)$ (transmitted) and $I_{\mathrm{r}}(t-\tau)$ (reference) are the intensities of two pulses involved in correlation process. τ is the time offset between the two pulse trains.

The difference of the interferometric cross-correlation from the intensity cross-correlation is that the underlying two electric fields which belong to individual pulse trains will interfere with each other. So what is measured is the interference intensity of the two pulse trains. Let the electric fields of the two optical pulses to be written in the conventional complex form as

$$E_{\mathrm{t,r}}(t) = \sqrt{I_{\mathrm{t,r}}(t)}\exp\left[-i\left(\omega_0 t - \phi_{\mathrm{t,r}}(t)\right)\right] \tag{5.2}$$

where $E_{\mathrm{t,r}}(t)$, $I_{\mathrm{t,r}}(t)$, ω_0 and $\phi_{\mathrm{t,r}}(t)$ denotes the electric field profiles, the intensity profiles, the carrier angular frequency and the arbitrary phases, respectively.

The interferometric cross-correlation signal could be expressed as

$$\begin{aligned} G_2(\tau) &= \int_{-\infty}^{+\infty} \left\{ \left[E_\mathrm{t}(t-\tau) + E_\mathrm{r}(t) \right]^2 \right\}^2 \mathrm{d}t \\ &= A(\tau) + \mathbf{Re}\left\{ 4\tilde{B}(\tau)\, e^{i\omega_0\tau} \right\} + \mathbf{Re}\left\{ 2\tilde{C}(\tau)\, e^{2i\omega_0\tau} \right\} \end{aligned} \tag{5.3}$$

where

$$A(\tau) = \int_{-\infty}^{+\infty} \left\{ E_\mathrm{t}^4(t-\tau) + E_\mathrm{r}^4(t) + 4E_\mathrm{t}^2(t-\tau)\, E_\mathrm{r}^2(t) \right\} \mathrm{d}t \tag{5.4a}$$

$$\tilde{B}(\tau) = \int_{-\infty}^{+\infty} \left\{ E_\mathrm{t}(t-\tau)\, E_\mathrm{r}(t) \left[E_\mathrm{t}^2(t-\tau) + E_\mathrm{r}^2(t) \right] \psi(t,\tau) \right\} \mathrm{d}t \tag{5.4b}$$

$$\tilde{C}(\tau) = \int_{-\infty}^{+\infty} \left\{ E_\mathrm{t}^2(t-\tau)\, E_\mathrm{r}^2(t)\, \psi^2(t,\tau) \right\} \mathrm{d}t \tag{5.4c}$$

$$\psi(t,\tau) = \exp\left\{ i\left[\phi_\mathrm{t}(t-\tau) - \phi_\mathrm{r}(t) \right] \right\} \tag{5.4d}$$

The purpose of the decomposition Eq. (5.3) is to show the three different frequency components centered respectively around zero, ω_0 and $2\omega_0$. Frequently, the correlation measurement system will act as a low pass filter, eliminating all terms but the Eq. (5.4a). The interferometric cross-correlation then reduces to the sum-frequency generation term and the background. That is actually just an intensity cross-correlation. The three terms $A(\tau)$, $\tilde{B}(\tau)$ and $\tilde{C}(\tau)$, which corresponds to respectively characteristic frequencies, could be extracted from the Fourier transform of the data.

To be more detailed, by observing at the expression of the Eq. (5.3), it is not hard to find the symmetric of the curve $G_2(\tau)$, which is a function of τ, the adjustable time delay between two pulses during measurement. The integrations over the 1st and the 2nd terms in the Eq. (5.4a) give constants and have nothing to do with τ. The 3rd term is basically the intensity correlation (labeled $A_c(\tau)$ in Eq. (5.1)). Assuming the transmitted and reference pulse trains having the same envelop ($E_t = E_r = E$), for large time offset between the two pulses, the intensity correlation term vanishes, leaving only the background of $2\int E^4 dt$, which is also the dc term in the interferometric correlation. In case of fully overlapping (the time offset between two pulses $\tau = 0$), Eq. (5.4a) reduces to $6\int E^4 dt$. Thus for the intensity correlation, the ratio of peak to background is 3 to 1. To take the fast oscillating terms $\tilde{B}(\tau)$ and $\tilde{C}(\tau)$ into account, the peak value becomes $16\int E^4 dt$. Thus it results in the ratio of peak to background of 8:1 for the interferometric correlation. Up to now, there is still a critical problem to our all-optical out-of-loop interferometric cross-correlation measurement method left to be addressed. In the Eq. 5.3 there are two oscillating terms, the 2nd term at the optical frequency ω_0 and the 3rd one at its second harmonic. So the final interferometric cross-correlation function will be the sum of two trigonometric functions running respectively at fundamental and the 2nd harmonic frequencies. Assuming the Gaussian shape pulses and using the parameters of the two pulses that we deal with in our experiment – reference pulse: 154 fs at 0.957 mW and transmitted pulse: 197 fs at 0.815 mW, the numerical integration over the Eq. 5.3 provides the expression of the interferometric cross-correlation signal as a function of the time delay between the two involved pulses (τ) as,

$$\begin{aligned} G_2(\tau) &= 340.767 + 335.455\exp\left(-\tau^2/62525\right) + \left[660.264\exp\left(-3\tau^2/219914\right)\right. \\ &+ \left. 686.749\exp\left(-3\tau^2/280286\right)\right]\cos\left(2\pi\tau/5.17\right) \\ &+ 670.91\exp\left(-\tau^2/62525\right)\cos^2\left(2\pi\tau/5.17\right) \end{aligned} \tag{5.5}$$

This simulated expression is shown in Fig. 5.6. Once we zoom in to the vicinity of $\tau = 0$, as shown in Fig. 5.1(a), it can be seen clearly from the signal's period of 5.17 fs, which corresponds to the light with the optical wavelength of 1550 nm, that the interferometric cross-correlation signal oscillates at the fundamental optical frequency but not at the frequency of $2\omega_0$. In other words, the fundamental term dominates. However, the flatter valleys, compared with the peaks, in Fig. 5.1(a) indicates the existence of the $2\omega_0$ term. This effect could be more clearly indicated in the 1^{st} order derivative of the interferometric cross-correlation signal with respect to the time delay (see Fig. 5.1(b)). The 1^{st} order derivative crossing zero means a extreme value position is passed in the original function. In Fig. 5.1(b), the difference between the ways that the slope function crossing the zero at the slope and at the valley is apparent. Even though, the existence of the $2\omega_0$ term will change nothing but push the maximum slope position slightly away from the middle point between two adjacent valley and peak positions toward the peak position. This phenomena will not affect our estimation of the jitter using the interferometric cross-correlation measurement.

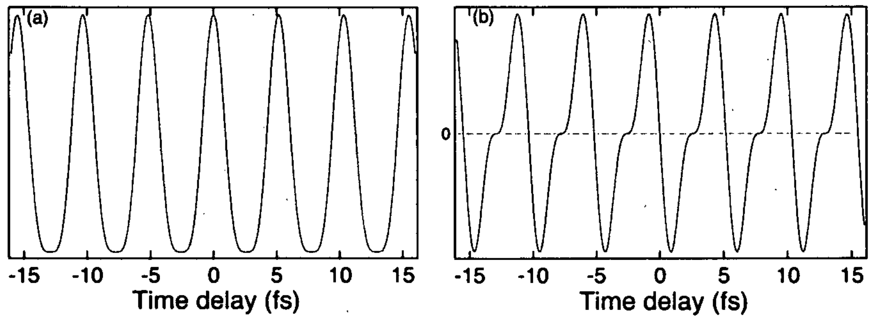

Figure 5.1: (a) The numerical simulation of the interferometric cross-correlation signal as a function of the time delay (τ) between the reference pulse (154 fs at 0.815 mW) and the transmitted pulse (197 fs at 0.957 mW) in the vicinity of $\tau = 0$. (b) The numerical simulation of the 1^{st} order derivative with respect to τ of the interferometric cross-correlation signal.

5.1.2 ICC using two photon absorption in Si-APD

We have discussed in section 2.4.4 that interferometric cross-correlation (collinear) has a better degree of sensitivity than the non-collinear approach. The reason is a single oscillatory cycle of the collinear approach represents a drift of the time offset between the two pulse trains of only 5.17 fs (one period of optical cycle at 1550 nm, the central wavelength for EDFL) while that of the non-collinear approach depends on the width of the pluses to be measured. In my case, as shown in the Fig. 5.5, the pulse width of the reference and transmitted arms are greater than 150 fs. So the slope at the half-maximum of the collinear correlation signal is approximately 30 times bigger than that of the non-collinear correlation signal. Thus collinear approach is about 30 times more sensitive than the non-collinear approach. However, this is just one of the advantages of the ICC approach for measuring the timing jitter.

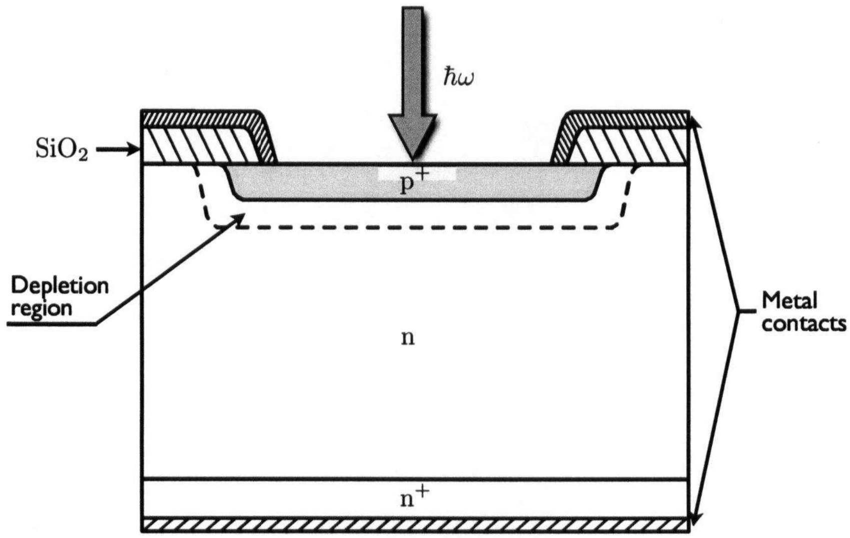

Figure 5.2: Typical silicon photodiode structure for photoconductive operation [39]

Two photon absorption (TPA) is applied herein for the ICC measurement of timing jitter. Before listing all kinds of advantages of measuring the ICC by using the TPA, first of all, let us explain what avalanche photodiode (APD) and two photon absorption is. In the first place, APD is a photodiode detector, which is a p-n junction structure where photons absorbed in the depletion region (5.2) generate electrons and holes which are subject to the local electric field within that layer. Because of this field, the two carriers drift in opposite directions and an electric current is induced in the external circuit [39].

Photodiodes have been fabricated from many of the semiconductor el-

(a)	II	III	IV	V	VI
		B	C	N	
		Al	Si	P	S
	Zn	Ga	Ge	As	Se
	Cd	In		Sb	Te

(b)	Elemental	IV compounds	Binary III-V compounds	Binary II-VI compounds
	Si	SiC	AlP	ZnS
	Ge	SiGe	AlAs	ZnSe
			AlSb	ZnTe
			GaN	CdS
			GaP	CdSe
			GaAs	CdTe
			GaSb	
			InP	
			InAs	
			InSb	

Table 5.1: Common semiconductor materials: (a) part of the Periodic Table where semiconductors occur; (b) elemental and compound semiconductors

ements listed in Table 5.1.2, as well as from compound semiconductors. Devices are often constructed in such a way that the light impinges normally on the p-n junction instead of parallel to it. A typical construction is seen in Fig. 5.2. There are three classical modes of photodiode operation: open circuit (photovoltaic), short circuit, and reverse biased (photoconductive). The APD works in the 3rd mode, in which a relatively large reverse bias ($\approx$ 10 Volts or more) is applied across the diode. Thus the external circuit current is directly proportional to the incident light irradiance. With sufficiently large reverse bias, the electrons and holes may acquire sufficient large energy to liberate more electrons and holes. Therefore, the internal amplification process happening in the diode is what causes it to be called an avalanche photodiode (APD).

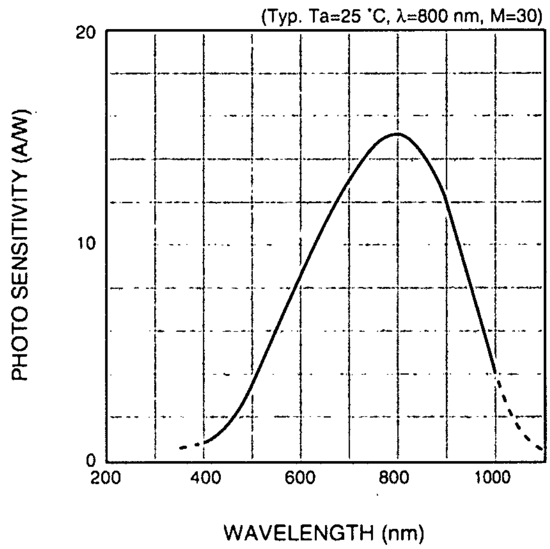

Figure 5.3: Spectral response of the Si-APD at 25°C

As for the for two-photo absorption (TPA), the classical definition defines it as the transition of an atom from its ground state to an excited state by simultaneous absorption of two laser photons [40]. The transition rate R due to TPA scales as the square of the laser intensity as

$$R = \frac{\sigma^{(2)} I^2}{\hbar\omega} \tag{5.6}$$

Due to its nonlinear characteristic, it was not observed until the invention of laser, which could provide the high enough power density to trigger the visible TPA process. In the case of TPA in APD, the energy difference between the conduction band and valence band is approximately twice as the energy of a single photon at the wavelength which is focussed on the APD. For example, in our experiment, we use Si-APD, which is sensitive to the wavelength around 800 nm as depicted in Fig. 5.3 [8], to receive the 1550 nm photons dumped from the Er^{3+} doped fiber laser.

TPA in GaAsP photodiode [41], AlGaAs light emitting diode [42] and Si avalanche photodiode (Si-APD) [43][44] have been used in 1997 for the autocorrelation measurement of femtosecond Ti:sapphire laser pulses at 800 nm (former two) and mode-locked semiconductor laser pulses at $1.5\,\mu m$ (last one). Here we borrow the TPA process, but to measure the timing jitter instead of measuring the pulse width. Although we do a different measurement, but we still share all the advantages of the TPA process for the ICC measurement. Primarily, there are three advantages of using APD instead of the conventional nonlinear crystal and PMT combination. In the first place, the nonlinear crystal approach is based on the second harmonic generation (SHG) which requires stringent phase-matching conditions and is hard to align. Secondly, due to the small conversion efficiency of the SHG over the short path length of the nonlinear crystal, PMT is needed to detect the generated harmonic signal. This dramatically increases the degree of complexity and the cost. Thirdly, the low resistance of the thin metallic film (that is used to replace the p-type or n-type layer in the p-n junction) and small sensitive area results in the small RC time constant thereby increasing the response speed of the detector. In our case, the Si-APD has a cut-off

[8] Reference to Hamamatsu datasheet of APD module C5460 series

frequency of 10 MHz. So far, we have not counted in the advantages of APD such as better stability , greater dynamic range and so on.

5.1.3 Fast Fourier transform on time signal

It has been introduced in section 2.4 that the synchronization stability in long distance transportation through optical fiber is often characterized by the integrated timing jitter over a certain frequency bandwidth. For getting the integrated jitter, we need to measure the jitter spectral density that is converted from phase spectral density by Eq. (2.17). In practice, we have two approaches to measure the phase spectral density. It can be measured directly by the FFT spectrum analyzer (Stanford Research Systems, Model No. SR780), but this only works in the frequency range from dc up to 102.4 kHz. However, a meaningful integrated jitter requires to be integrated up to the order of magnitude of Nyquist frequency of the fiber laser, which is used to generate the pulse trains. In our case, the Nyquist frequency is 25 MHz, half of the repetition rate. Therefore, for the frequency range between 102.4 kHz and $\sim$ 10 MHz[9], the data needs to be collected by the oscilloscope in time domain and then transformed into frequency domain manually. So in this section in the following, we will talk about the general process of this transformation. Because, in reality, data collected at a certain sampling rate (set by the oscilloscope) are discrete, but not continuous. We will apply discrete Fourier transform (DFT) on the time scale measurements.

[9]Merely measuring up to 10 MHz is due to the cut-off frequency of 10 MHz of APD that I use.

Eq. (5.7) shows the FFT [45], which is one of the kinds of DFT.

$$F_{\nu_s} = \frac{1}{n}\sum_{r=1}^{n}\left\{f_{t_r}\exp\left[\frac{2\pi i\,(r-1)\,(s-1)}{n}\right]\right\} \tag{5.7}$$

where f_{t_r} is a series of data in the time domain, r is the index of them, F_{ν_s} is the corresponding series of data in the frequency domain, s is the index of them, n is the total number of data in the series.

In the follow step, we average the value of each discrete frequency component over the next interval between two adjacent frequency components to convert the discrete series into continuous density function [46]. In the Eq. (5.8), t_1 and t_n are the starting time and ending time of the measurement, respectively. Therefore the minimum frequency component (the interval between frequency component as well), at which the signal strength can be derived by Fourier transform, is $1/\left|t_n - t_1\right|$ $F(\nu)$ gives the spectrum strength at each Fourier frequency ν in a measurement bandwidth of 1 Hz and has a unit of Volt/Hz.

$$F(\nu) = \frac{F_{\nu_s}}{1/\left|t_n - t_1\right|}\left[\frac{\text{Volt}}{\text{Hz}}\right] \tag{5.8}$$

From the spectrum expression $F(\nu)$, we can compute the one-side power spectral density (PSD), $\mathrm{PSD}(\nu)$ in Volt^2/Hz as

$$\mathrm{PSD}(\nu) = \frac{2F(\nu)^2}{\left|t_n - t_1\right|} = \tilde{A}(\nu)^2\left[\frac{\text{Volt}^2}{\text{Hz}}\right] \tag{5.9}$$

where $\tilde{A}(\nu)$ is defined in the Eq. (2.17) as the measured error signal as a function of frequency, from which we can compute the jitter spectral density

(JSD), and then the integrated jitter. The factor of 2 in the definition of PSD is due to adding the contributions from both positive and negative frequencies. The physical meaning of PSD is that divides the total power of one pulse of the train (optical frequency comb). We can clearly see this from the integration of PSD over its entire one-sided frequency domain (Eq. (5.10)).

$$\int_0^{\nu_\mathrm{h}} \mathrm{PSD}(\nu)\,\mathrm{d}\nu = \int_0^{\nu_\mathrm{h}} 2\,|F(\nu)|^2 / (t_\mathrm{n} - t_1)\,\mathrm{d}\nu =$$
$$= 1/(t_\mathrm{n} - t_1) \times \int_{-\nu_\mathrm{h}}^{+\nu_\mathrm{h}} |F(\nu)|^2\,\mathrm{d}\nu = 1/(t_\mathrm{n} - t_1) \times \int_{t_1}^{t_\mathrm{n}} |f(t)|^2\,\mathrm{d}t \quad (5.10)$$

5.1.4 All-optical jitter measuring setup

The experimental setup for the all-optical jitter measurement is depicted in the Fig. 5.4. One output of the beam splitter is sent to this jitter measuring setup for the independent all-optical out-of-loop jitter measurement by the interferometric cross-correlation with Si-APD. Because the reference beam is passed through the polarizing beam splitter (PBS) while the transmitted beam is reflected back by the PBS, so they are vertically and horizontally polarizing respectively. Therefore they can be decoupled [10] and split into two arms again by the first PBS in the jitter measurement alignment. The delay line located in one of the arm could adjust the time offset between the two pulse trains. The delay line is basically a translation stage. A PZT located under the translation stage and between the micrometer head and the movable part provides the capability of fine adjustment. At the 2$^{\mathrm{nd}}$ PBS they are re-coupled and then forced to the same polarization by the

[10] Extinction ratio of the PBS that I use is 500 : 1.

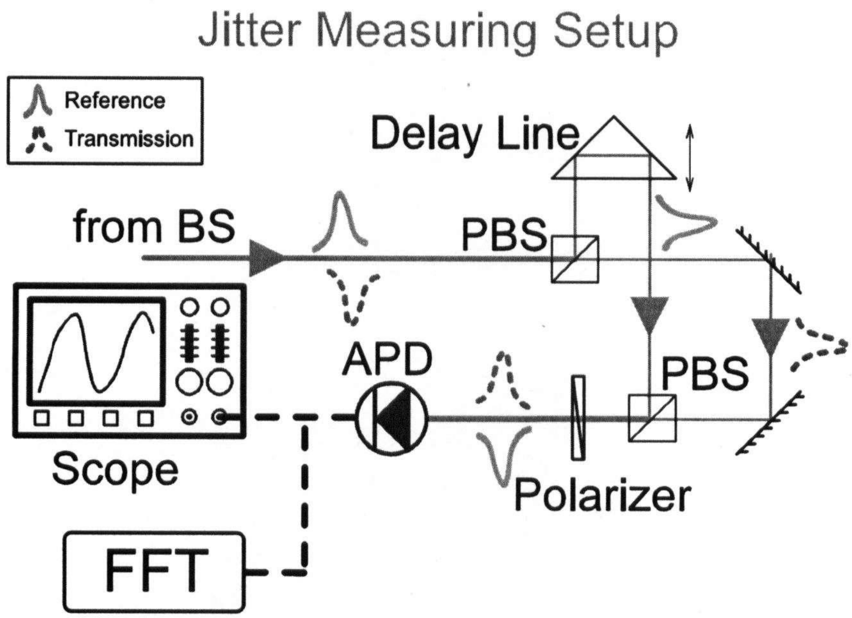

Figure 5.4: Experimental configuration of the interferometric cross-correlation (ICC) measurement of the transmission timing jitter of the transmitted signal with respect to the reference signal. BS, beam splitter; PBS, polarizing beam splitter; APD, avalanche photodiode; FFT, fast Fourier transform spectrum analyzer.

polarizer afterwards. In this way, the interference between the two pulses is maximized. In fact, a convex lens is located between the polarizer and the Si-APD to focus the beam onto the its sensitive face. This method will greatly improve the ICC signal strength from the Si-APD due to the nonlinear characteristics. The spectral density from dc to 102.4 kHz is measured by the FFT spectrum analyzer and higher frequency part is measured by the oscilloscope at different time scales.

5.2 Experimental results

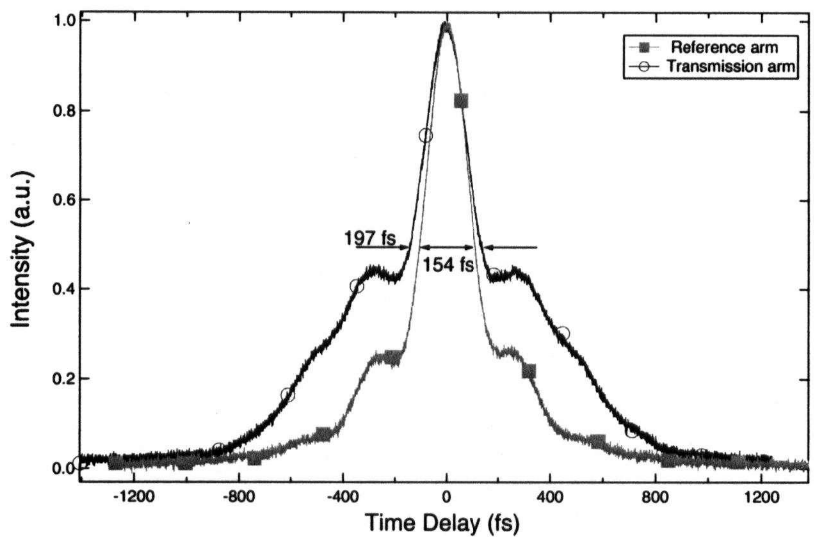

Figure 5.5: Intensity auto-correlation measurement of the pulse widths of the reference arm (red curve with filled square) and transmission arm (blue curve with open circle). One arm of the auto-correlator used to do the measurement is periodically scanning back and forth over the length of the other arm. That results in the symmetric curves measured. Given the Gaussian shape of pulses in the time domain, the pulse widths of the reference and transmission arms are 154 fs and 197 fs, respectively.

As shown in the Fig. 5.5, the pulse widths of reference and transmitted pulses are measured through the intensity auto-correlation. The length of one arm of the auto-correlator is scanning back and forth over the length of the other arm by rotating a pair of parallel motor-driven mirrors, which continuously and periodically change the optical length of the arm that they are located in. The pulse widths of the reference and transmitted pulses are 154 fs and 197 fs, respectively, while the transform limit pulse width (spectrum ranging from 1520 nm to 1580 nm) is 57 fs given the Gaussian-shaped pulse ($\Delta\nu\,\Delta\tau \geq 0.441$ [38]). So the pulses are far from perfectly compressed back to the transform limit. This can also be seen from the shoulders in the intensity auto-correlation pattern of the transmission signal in the Fig. 5.5 and even the reference signal as well.

5.2.1 Scheme 1: spectral leveraging

In previous remote transfer experiments, the perfect envelope shape is quite important for conducting the intensity cross-correlation jitter measurement, because the slope of the envelope line is used to calculate the timing jitter. On one hand, we want to compress it back to a better shape (e.g. Gaussian shape) because we need to assume a shape of the envelope of the pulse so that with using the parameters, such as the pulse width and peak intensity, the slope for calculating the timing jitter can be worked out from the model. On the other hand, the better the pulse is compressed, the narrower and higher the pulse is hence larger slope, which is preferred for getting the timing jitter with high accuracy. While in the measurement approach using ICC, we needn't to worry too much about compressing the pulse back to the non-chirped transform limit pulse, we still need to compress the pulse as short as possible to get a bigger signal to noise ratio. I simulated the ICC signal in Mathematica using the Gaussian shape pulses and the single frequency spectrum corresponding to 1550 nm. The electric field of the pulse can be expressed as,

$$E_{\mathrm{t,\,r}}(t) = A_{\mathrm{t,\,r}} \exp\left[-\frac{t^2}{2\sigma^2_{\mathrm{t,\,r}}}\right] \exp\left[i\left(\omega_0 t - \phi_{\mathrm{t,\,r}}(t)\right)\right] \tag{5.11}$$

where the subscript t and r represent transmitted and reference signals, $A_{\mathrm{t,\,r}}$ the peak amplitude, $\sigma_{\mathrm{t,\,r}}$ is the full width at half maximum (FWHM) of the Gaussian-shaped pulse, ω_0 is the carrier frequency, $\phi_{\mathrm{t,\,r}}(t)$ is the random phase.

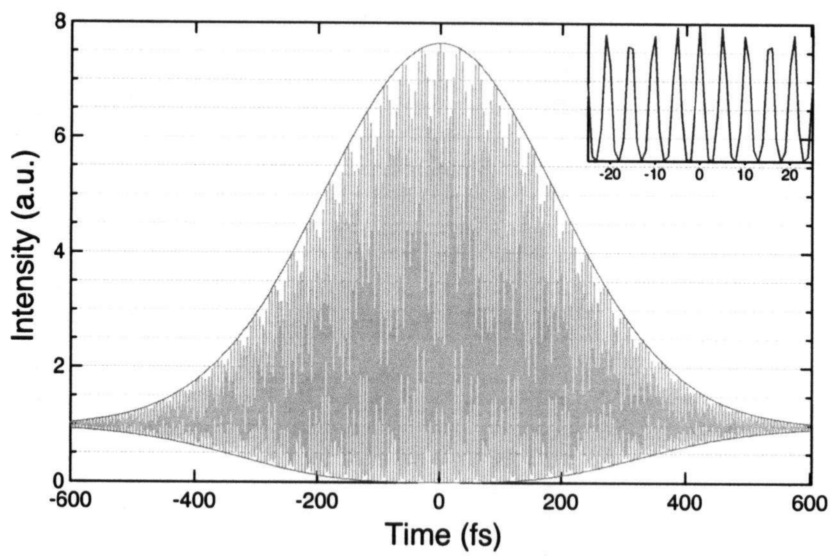

Figure 5.6: The simulated interferometric cross-correlation pattern of a 154 fs pulse and a 197 fs pulse without considering the possible existing chirp in pulses. The peak-to-background ratio of $\sim$ 7.6, but not the usual 8 [38], is due to considering the different intensities of two interfering pulse trains. The envelope of the interaction pattern is represented by the red solid line. The inset shows the zoomed-in pattern around the offset of 0.

In the section 5.1.1, we have introduced the mathematical derivation of the interferometric correlation. However, as considering the different intensities (pulse widths) of 0.957 mW (154 fs) and 0.815 mW (197 fs) of the reference and transmitted pulses, the peak-to-background ratio reduces slightly from 8 to 7.6 as depicted in the Fig. 5.6. The inset in the Fig. 5.6 zooms in to the position around the peak. The uneven look of the curve is due to the not high enough sampling rate and it is supposed to look smooth. The oscillatory cycle of the ICC pattern (interval between two adjacent peaks) is 5.17 fs, which is the oscillating period of the 1550 nm infrared radiation. We can find the approximate period from the inset's horizontal axis, which is in femtosecond. In fact, the spectrum is not just a single frequency and ranges from $\sim$ 1520 nm to $\sim$ 1580 nm. Also, the existence of the chirp and sequentially the pre-pulse of the measured ICC pattern with Si-APD cause the pulse to no longer have the Gaussian shape. But what we are going to use is any one single oscillating peak around the main peak as shown in the insets of Figs. 5.6 as long as the synchronization scheme is good enough that it could limit the timing jitter smaller than 5.17 fs, the interval between two adjacent peaks of the ICC signals. A problem appearing due to the multi-frequencies existing in the spectrum is that it is possible for the time interval between two adjacent peaks to be slightly different from 5.17 fs. But since the spectrum is not very wide (1520 nm $\sim$ 1580 nm), the largest possible relative error is only 2%.

The synchronization quality between the reference and the transmitted signals is always reported as an integrated timing jitter over a bandwidth from several mHz or several Hz to the same order of magnitude as the

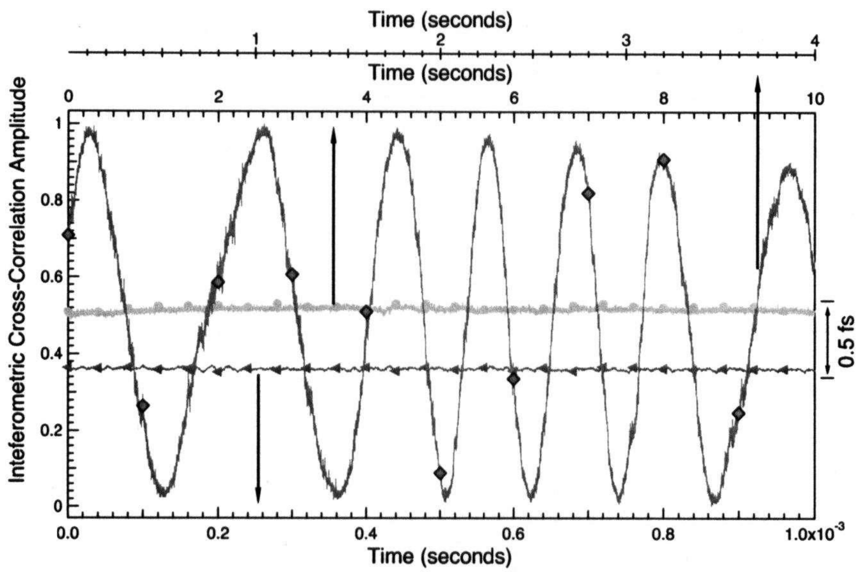

Figure 5.7: Time domain traces of the interferometric cross correlation signal between the reference and transmitted pulses. The green (with filled circle) and blue (with filled triangle) curves show the noise measured respectively for 10 s and 1 ms intervals when it is actively canceled by the approach of spectral leveraging (scheme 1). The equivalent time scale is shown on the right axis. The red curve is the free-running noise.

repetition rate of the pulse trains. The ICC signal from the Si-APD is measured by the FFT spectrum analyzer and oscilloscope as well depending on the frequency range in which the signal is to be measured. In order to cover the whole frequency bandwidth in which we are interested, the oscilloscope is set at the sampling rate of 10^3 per division. And the ICC signal is recorded at the time scales of 1 second/div, 0.4 second/div, 4×10^{-2} second/div, 4×10^{-3} second/div, 10^{-3} second/div, 10^{-4} second/div and $5 \times 10^{-}5$ second/div. A few representative time domain traces from the APD as recorded on a digital oscilloscope are shown in Fig. 5.7. The unlocked signal is shown in red with filled diamond and its amplitude is normalized to 1. At t=0, the pulses are overlapped and then drift apart due to environmental perturbations in the $\sim$ 60-m optical fiber path length. In this signal, a single oscillatory cycle represents a drift of 5.17 fs (one period of an optical cycle at 1550 nm). As the pulses drift away from maximal overlap, the (nonlinear) TPA signal goes down, leading to a reduction in the peak amplitude after every cycle. When the PLL is activated using spectral leveraging (scheme 1), the measured ICC signal is shown by the blue and green traces corresponding to two difference time scales. In both of these traces the initial timing offset is adjusted to approximately the half intensity level of the ICC signal for maximum sensitivity. It is clear from these traces that a tight lock is established.

In the definition of the integrated timing jitter in Eq. 2.17, the nominal central frequency ν_0 in our case is on the order of $\sim$200 THz (optical frequency of the EDFL) leading to a substantially increased sensitivity for the jitter measurement. A frequency domain measurement of the ICC signal followed by the analysis shown by Eq. (2.17) and (2.18) provides the jitter spectral density and total rms jitter measured out-of-loop. The results are shown in Fig. 5.8 for scheme 1. Also shown is the noise floor of the APD. The corresponding total rms timing jitter is shown in Fig. 5.8 by the identical color but dashed curve. An rms timing jitter of 11.4 as (1 Hz to 10 MHz) is measured when locked by spectral leverage setup (scheme 1). The noise floor of APD (blue curve in Fig. 5.8) is 9.7 as (1 Hz to 10 MHz). It is easy

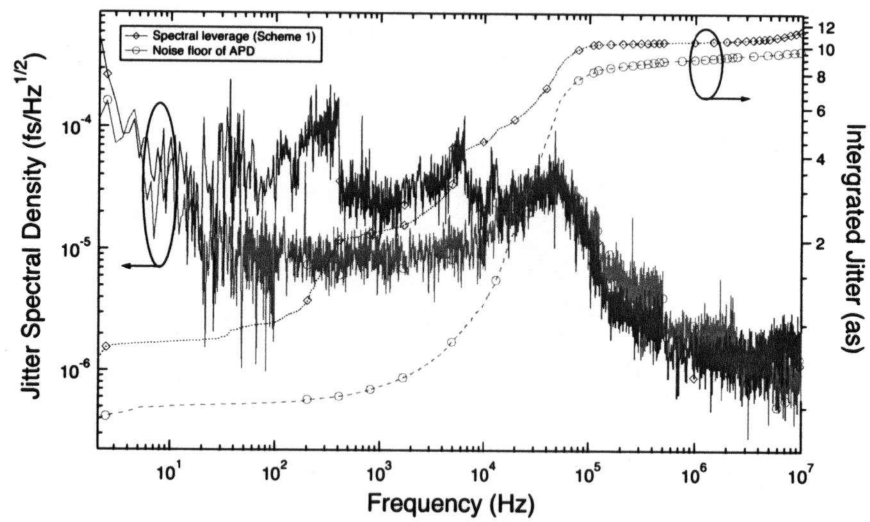

Figure 5.8: All-optical out-of-loop measurement of power spectral density (solid curves referring to left axis) and integrated jitter (dashed curves referring to right axis) of APD's noise floor and noise when actively canceled by the approach of spectral leverage (scheme 1).

to see both schemes cancel the noise almost to the noise floor of the ICC measurement itself. Moreover, these out-of-loop measurements of the jitter compare well with the measured in-loop measurements reported earlier. It is also worth noting that instead of using the ICC to independently measure the jitter, the ICC signal itself could be employed to generate an (all-optical) error signal with a sensitivity and noise floor comparable to schemes 1 and 2.

5.2.2 Scheme 2: simple optical heterodyne

The results are shown in Fig. 5.9 for scheme 2. Also shown is the noise floor of the APD. The corresponding total rms timing jitter is shown in Fig. 5.9

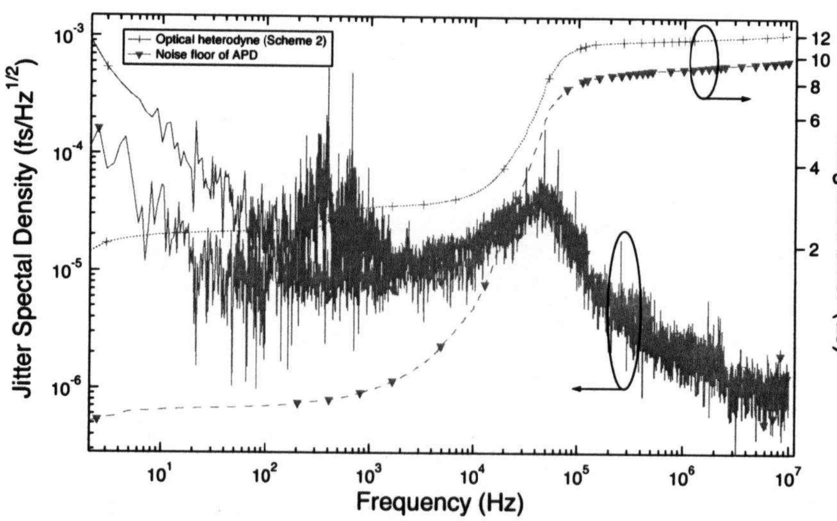

Figure 5.9: All-optical out-of-loop measurement of power spectral density (solid curves referring to left axis) and integrated jitter (dashed curves referring to right axis) of APD's noise floor and noise when actively canceled by the approach of optical heterodyne (scheme 2).

by the identical color but dashed curve. An rms timing jitter of 12.1 as (1 Hz to 10 MHz) is measured when locked by the optical heterodyne setup (scheme 2). The noise floor of APD (blue curve in Fig. 5.9) is 9.7 as (1 Hz to 10 MHz). It's easy to see both schemes cancel the noise almost to the noise floor of the ICC measurement itself. In another way, successfully actively locking the transmitted pulse train to the reference one proves that it is appropriate to assume the offset frequency keeps unchanged when traveling down through $\sim$ 60 m fiber.

Moreover, these out-of-loop measurements of the jitter compare well with the measured in-loop measurements reported earlier. It is also worth noting that instead of using the ICC to independently measure the jitter, the ICC

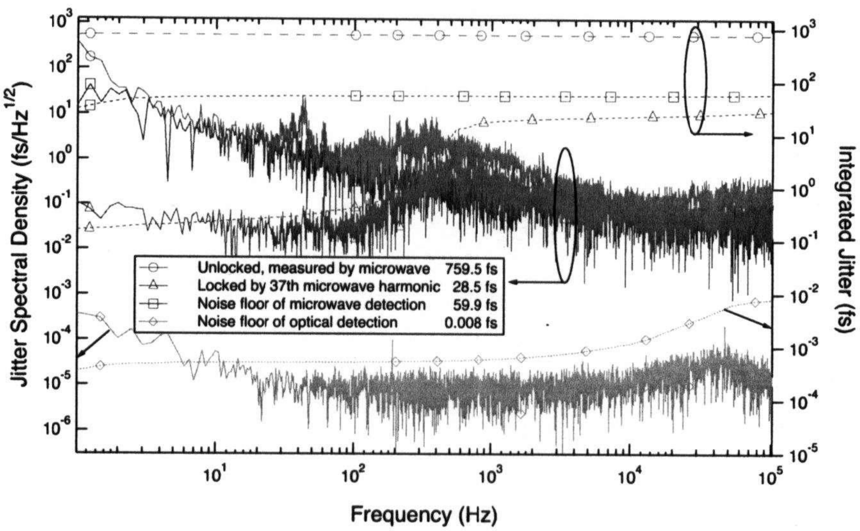

Figure 5.10: Power spectral density (solid curve referring to left axis) and integrated jitter (dashed curve referring to right axis) of unlocked noise, noise floor of microwave detection and that of optical detection. Microwave detection is conducted at 1822.46 MHz, the 37$^{\text{th}}$ harmonic of the repetition rate of the mode-locked fiber laser.

signal itself could be employed to generate an (all-optical) error signal with a sensitivity and noise floor comparable to schemes 1 and 2.

5.2.3 Improvements offered by all-optical approaches

To illustrate the improvement offered by our all-optical approaches both in the detection and error signal generation, we also locked the same $\sim$ 60-m fiber link with the standard microwave approach. Similar to Ref. [7], the transmitted and reference pulse signals were individually detected at 1.822 GHz (the 37$^{\text{th}}$ harmonic). The resulting signals were mixed in the microwave domain to generate an error signal. The jitter spectral density under various conditions is shown in Fig. 5.10. Note that the upper frequency limit in this figure is only 100 kHz. The red curve shows the measured, unlocked jitter spectral density, which yields 760 fs (1 Hz to 100 kHz). When this microwave generated error signal is used in conjunction with the PLL, the locked jitter spectral density (purple curve) is measured, giving a rms jitter of 28.5 fs (1 Hz to 100 kHz). The fact that the locked signal is below the noise floor at certain frequencies indicates an out-of-loop measurement is required to truly measure the jitter. Nevertheless, when these curves are compared with the noise floor of the ICC signal, (green curve, re-plotted from Figs. 5.8 and 5.9) the vast improvement in the sensitivity of the jitter measurement by all-optical means is clear. The comparison between the two techniques in Fig. 5.10 provides quantitative confirmation that, as was suspected in previous investigations [7], a significant portion of the measured jitter was in fact caused by the microwave measurement technique itself.

In addition, when the PLL is locked using these microwave signals, the ICC signal continues to oscillate (similar to the red curve in Fig. 5.7) with a increased amount of high frequency components, indicating a large amount (> 5 fs) of uncompensated jitter. This observation verifies the independent integrated rms jitter results shown in Fig. 5.10. More importantly, it also provides another indication of the superiority provided by the all-optical locking schemes shown in Figs. 3.1 and 4.1.

Chapter 6

Project summary and future work

6.1 Summary

Two different all-optical techniques for distributing an ultra-low jitter frequency standard are experimentally demonstrated. In this work, a high-stability, low jitter rf signal is transmitted over $\sim$ 60-m fiber link with a jitter of 11.4 as (1 Hz to 10 MHz) using spectral leveraging scheme representing a three order of magnitude improvement over previously reported results. The simple optical heterodyne scheme performs a transmitted jitter of 12.1 as (1 Hz to 10 MHz). These performance levels are measured out-of-loop by an interferometric cross correlation. The key for realizing this result is the vast reduction in the noise floor (to 9.7 as) of both the error signal generation and measurement techniques via all-optical methods.

6.2 Transferring reference signal through longer fiber

For this first demonstration we have transmitted over a 60-m optical fiber link. Future work will entail extending this distance to $>$ 10 km and we are optimistic that a similar level of performance will be achieved for this longer transmission distance for two reasons. When we used the standard microwave phase detection technique, the jitter performance (Fig. 5.10) of this 60-m link is similar to previously reported results over distances of 9.1 km [7]. This indicates the 9.1-km link jitter performance is most certainly limited by the microwave detection method. Second, the additional noise experienced along a longer transmission distance will be predominated environmental (i.e., low frequency, $<$ 10 kHz) in nature. Such noise can be corrected by common piezo-electric transducers similar to the devices used in this work. However, for the all-optical approach presented herein to be successfully applied to longer transmission distances, the additional accumulated dispersion and loss experienced by the transmitted signal will be need to be addressed.

6.3 Improving all-optical measurement by using birefringent filter

For the current all-optical out-of-loop jitter measuring setup, even though the measured jitter could be as low as 11.2 as while being integrated from 1 Hz to 10 MHz with a noise floor of only 9.7 as, there still may be extra noise introduced in by the bulk optics setup (translation stage, mirror mounts, et al.), which always oscillate in small amount, and the air flow when transmitting the pulse trains from the beamsplitter to the Si-APD in free space (reference to Fig. 5.4). In the current setup, the light need to travel scores of centimeters and is reflected four to five times before being detected by the Si-APD using the ICC finally. In other words, we measured the integrated jitter of the transmitted pulse plus the extra noise introduced in by the measuring setup. Therefore, in order to reduce the extra noise to be as low as possible, we want a measuring facility with simple setup, short optical length and small amount of bulk optics.

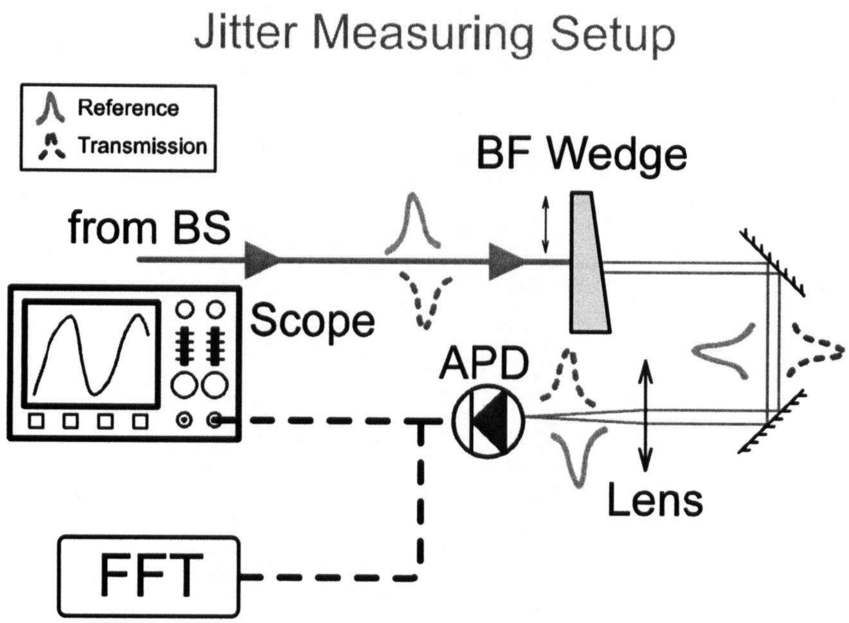

Figure 6.1: Experimental configuration of the interferometric cross-correlation (ICC) measurement of the transmission timing jitter of the transmitted signal with respect to the reference signal using birefringent filter. BF, birefringent filter; APD, avalanche photodiode; FFT, fast Fourier transform spectrum analyzer.

Birefringent filter (BF) is a good candidate. As shown in Fig. 6.1, the BF is able to be used instead of the pair of PBSs. The BF is able to be made in a wedge shape. By using the translation stage located under the wedge, the thickness of the BF in the optical path is able to be adjusted. From the beamsplitter, the reference and the transmitted pulse trains are polarized horizontally and vertically, respectively. Because the refractive indices of the BF are different in the ordinary and extraordinary polarization directions, so the two pulse trains could be offset in time by some amount after passing through the BF by lining up the BF with the polarization of one of the pulse trains. The two pulse trains will also be shifted in space by the wedge-shaped BF, therefore, a convex lens is used to focus them onto the sensitive surface of the APD to realize the ICC measurement as done before. The two mirrors in Fig. 6.1 are not necessary. They just make the drawing look better.

We could choose the BF which is made of crystal quartz. The commercial product is available from CVI and VLOC. The minimal available thickness is ~ 0.5 mm. From the product catalogue of CVI, the ordinary and extraordinary refractive indices of crystal quartz at 1550 nm are $n_\mathrm{o} = 1.52761$ and $n_\mathrm{e} = 1.53596$. If the thickness of the BF is d, the time offset provided by that is able to be expressed,

$$\delta\tau = \frac{|n_\mathrm{e} - n_\mathrm{o}|\, d}{c} = \frac{(1.53596 - 1.52761) \times 0.5\,\mathrm{mm}}{2.998 \times 10^{8}\,\mathrm{m/s}} = 13.9\,\mathrm{fs} \tag{6.1}$$

where c is the speed of light in free space. We can see 0.5 mm of this type of crystal quartz provides time offset of 13.9 fs, which is about two oscillatory period of the interferometric cross-correlation signal at 1550 nm, between two pulse trains. So to set the thin end of wedge to be 0.5 mm and thick end to be 1 nm can provide a dynamic range of 13.9 fs for the time delay between two pulse trains by adjusting the translation stage located underneath the wedge-shaped BF. Therefore, when the transmitted signal is synchronized to the reference one, we can make the ICC signal at the half-peak value, where gives the highest sensitivity, by changing the thickness of BF in the way of the light thus the time offset between two pulse trains.

However, there is an intrinsic limitation of the ICC jitter measurement scheme. The jitter measured by the ICC is caused by two factors. One of them is the jitter in envelope arrival times of two pulse trains [38] while the other is the change in the difference of the carrier-envelope-offset frequencies of the two pulse trains [25]. In our case where the two combs are derived from the same laser, the latter factor can be neglected as it would have to be caused by a rapid time-varying change in the fiber dispersion.

6.4 Locking repetition rates of two mode-locked lasers

Lastly, while we demonstrated these new all-optical approaches within the context of remote frequency transfer, the spectral leveraging locking technique (scheme 1 in Fig. 3.1) as well as the ICC measurement procedure could be easily and transparently be applied to synchronization of independent (local and remote) fs lasers as long as the difference of the two-carrier-envelope-offset frequencies is passively stable enough such that optical heterodyne signal won't fall out of the bandpass filter's (BPF) bandwidth (see Fig. 3.1) and we would expect a similar level of jitter performance. A BPF which has a compatible bandwidth with the repetition rate of the mode-locked fiber lasers that we are working on is preferred in order to avoid the optical heterodyne signals being filtered out.

Bibliography

[1] J. Levine, "Introduction to time and frequency metrology," Rev. Sci. Instrum. **70**(6), 2567–2596 (1999).

[2] S. A. Diddams, J. C. Bergquist, S. R. Jefferts, and C. W. Oates, "Standards of time and frequency at the outset of the 21st century," Science **306**(5700), 1318–1324 (2004).

[3] A. D. Ludlow, M. M. Boyd, T. Zelevinsky, S. M. Foreman, S. Blatt, M. Notcutt, T. Ido, and J. Ye, "Systematic study of the ^{87}Sr clock transition in an optical lattice," Phys. Rev. Lett. **96**, 033,003 (2006).

[4] B. Shillue, S. AlBanna, and L. D'Addario, "2004 IEEE International Topical Meeting on Microwave Photonics Technical Digest," in *Transmission of low phase noise, low phase drift millimeter-wavelength references by a stabilized fiber distribution system*, 2004 IEEE International Topical Meeting on Microwave Photonics Technical Digest, pp. 201–204 (Institute of Electrical and Electronics Engineers, Piscataway, New Jersey, 2004).

[5] "Linac Coherent Light Source - LCLS," URL `http://www-ssrl.slac.stanford.edu/lcls/index.html`.

[6] M. Calhoun, R. Sydnor, and W. Diener, "A stabilized 100-Megahertz and 1-Gigahertz reference frequency distribution for Cassini radio science," Interplanetary Network Progress Rep. 42-148, Jet Propulsion Laboratory, Pasadena, California (2002).

[7] K. W. Holman, D. D. Hudson, J. Ye, and D. J. Jones, "Remote transfer of a high-stability and ultralow-jitter timing signal," Opt. Lett. **30**(10), 1225–1227 (2005).

[8] S. M. Foreman, K. W. Holman, D. D. Hudson, D. J. Jones, and J. Ye, "Remote transfer of ultrastable frequency references via fiber networks," Rev. Sci. Instrum. (to be published).

[9] T. R. Schibli, J. Kim, O. Kuzucu, G. J. T., S. N. Tandon, G. S. Petrich, L. A. Kolodziejski, J. G. Fujimoto, E. P. Ippen, and F. X. Kaertner, "Attosecond active synchronization of passively mode-locked lasers by balanced cross correlation," Opt. Lett. **28**, 947–949 (2003).

[10] A. Bartels, S. A. Diddams, T. M. Ramond, and L. Hollberg, "Mode-locked laser pulse trains with subfemtosecond timing jitter synchronized to an optical reference oscillator," Opt. Lett. **28**, 663–665 (2003).

[11] J. Ye, J. L. Peng, R. J. Jones, K. W. Holman, J. L. Hall, D. J. Jones, S. A. Diddams, J. Kitching, S. Bize, J. C. Bergquist, L. W. Hollberg, L. Robertsson, and L.-S. Ma, "Delivery of high-stability optical and microwave frequency standards over an optical fiber network," J. Opt. Soc. Am. B **20**(7), 1459–1467 (2003).

[12] C. J. Koester and E. Snitzer, "Amplification in a fiber laser," Appl. Opt. **3**(10), 1182–1186 (1964).

[13] L. E. Nelson, "Mode-locking of thulium-doped and erbium-doped fiber lasers," Ph.D. thesis, Massachusetts Institute of Technology (1997).

[14] F. Adler, K. Moutzouris, A. Leitenstorfer, H. Schnatz, B. Lipphardt, G. Grosche, and F. Tauser, "Phase-locked two-branch erbium-doped fiber laser system for long-term precision measurements of optical frequencies," Opt. Express **12**(24), 5872–5880 (2004).

[15] H. A. Haus, K. Tamura, L. E. Nelson, and E. P. Ippen, "Stretched-pulse additive pulse mode-locking in fiber ring lasers: theory and experiment," IEEE J. Quantum Electron. **31**(3), 591–598 (1995).

[16] H. A. Haus, J. G. Fujimoto, and E. P. Ippen, "Structures for additive pulse mode locking," J. Opt. Soc. Am. B **8**(10), 2068–2076 (1991).

[17] K. Tamura, H. A. Haus, and E. P. Ippen, "Self-starting additive pulse mode-locked erbium fibre ring laser," Electron. Lett. **28**(24), 2226–2228 (1992).

[18] L. E. Nelson, D. J. Jones, K. Tamura, H. A. Haus, and E. P. Ippen, "Ultrashort-pulse fiber ring lasers," Appl. Phys. B **65**(2), 277–294 (1997).

[19] K. Tamura, J. Jacobson, E. P. Ippen, H. A. Haus, and J. G. Fujimoto, "Unidirectional ring resonators for self-starting passively mode-locked lasers," Opt. Lett. **18**(3), 220–222 (1993).

[20] G. P. Agrawal, *Nonlinear Fiber Optics*, chap. 5, pp. 135–202, Optics and Photonics (Academic Press, San Diego, 2001).

[21] G. P. Agrawal, *Nonlinear Fiber Optics*, chap. 1, pp. 1–30, Optics and Photonics (Academic Press, San Diego, 2001).

[22] K. R. Tamura, "Additive Pulse Mode-locked Erbium-Doped Fiber Lasers," Ph.D. thesis, Massachusetts Institute of Technology (1994).

[23] W. H. Knox, "In situ measurement of complete intracavity dispersion in an operating Ti:sapphire femtosecond laser," Opt. Lett. **17**(7), 514–516 (1992).

[24] J. N. Eckstein, A. I. Ferguson, and T. W. Hänsch, "High-resolution two-photon spectroscopy with picosecond light-pulses," Phys. Rev. Lett. **40**(13), 847–850 (1978).

[25] D. J. Jones, S. A. Diddams, J. K. Ranka, A. Stentz, R. S. Windeler, J. L. Hall, and S. T. Cundiff, "Carrier-envelope phase control of femtosecond mode-locked lasers and direct optical frequency synthesis," Science **288**(5466), 635–639 (2000).

[26] L.-S. Ma, P. Jungner, J. Ye, and J. L. Hall, "Delivering the same optical frequency at two places: Accurate cancellation of phase noise introduced by an optical fiber or other time-varying path," Opt. Lett. **19**(21), 1777–1779 (1994).

[27] D. D. Hudson, S. M. Foreman, S. T. Cundiff, and J. Ye, "Synchronization of mode-locked femtosecond lasers through a fiber link," Opt. Lett. **31**(13), 1951–1953 (2006).

[28] K. W. Holman, "Distrubution of an Ultrastable Frequency Reference Using Optical Frequency Combs," Ph.D. thesis, University of Colorado (2004).

[29] D. W. Allan, "Statistics of atomic frequency standards," Proc. IEEE **54**, 221 (1966).

[30] F. L. Walls, "Laser Frequency Stabilization, Standards, Measurement, and Applications," in *Phase noise issues in femtosecond lasers*, J. L. Hall and J. Ye, eds., vol. 4269 of *Proceedings of SPIE*, pp. 170–177 (SPIE, 2001).

[31] L. S. . Ma, R. K. Shelton, H. C. Kapteyn, M. M. Murnane, and J. Ye, "Sub-10-femtosecond active synchronization of two passively mode-locked Ti:sapphire oscillators," Phys. Rev. A **64**(2), 021,802 (2001).

[32] R. K. Shelton, S. M. Foreman, L.-S. Ma, J. L. Hall, H. C. Kapteyn, M. M. Murnane, M. Notcutt, and J. Ye, "Subfemtosecond timing jitter between two independent, actively synchronized, mode-locked lasers," Opt. Lett. **27**(5), 312–314 (2002).

[33] T. R. Schibli, J. Kim, O. Kuzucu, J. T. Gopinath, S. N. Tandon, G. S. Petrich, A. Kolodziejski, J. G. Fujimoto, E. P. Ippen, and F. X. Kärtner, "Attosecond active synchronization of passively mode-locked lasers by balanced cross correlation," Opt. Lett. **28**, 947–949 (2003).

[34] A. Bartels, S. A. Diddams, T. M. Ramond, and L. Hollberg, "Mode-locked laser pulse trains with subfemtosecond timing jitter synchronized to an optical reference oscillator," Opt. Lett. **28**(8), 663–665 (2003).

[35] J. Ye and S. T. Cundiff, "Femtosecond Optical Frequency Comb Technology: Principle, Operation, and Applications," in *Optical frequency combs and their applications*, J. Ye and S. T. Cundiff, eds., pp. 12–53 (Springer, 2005).

[36] G. P. Agrawal, *Nonlinear Fiber Optics*, Optics and Photonics (Academic Press, San Diego, 2001).

[37] In an actual implementation of remote synchronization, a portion of the delivered signal will be retro-reflected back and compared with the reference signal.

[38] J.-C. Diels and W. Rudolph, *Ultrashort Laser Pulse Phenomena: Fundamentals, Techniques, and Applications on a Femtosecond Time Scale*, Optics and Photonics (Academic Press, San Diego, 1996).

[39] K. J. Gåsvik, *Optical Metrology (3rd edition)* (Wiley, West Sussex, 2002).

[40] R. W. Boyd, *Nonlinear Optics* (Academic Press, 2003).

[41] J. K. Ranka, A. Gaeta, A. Baltuska, M. S. Pshenichnikov, and D. A. Wiersma, "Autocorrelation measurement of 6-fs pulses based on the two-photon-induced photocurrent in a GaAsP photodiode," Opt. Lett. **22**, 1344–1346 (1997).